PFC/RR-92-11

A High-Power 95 GHz Gyro-TWT Amplifier

Kreischer, K.E.; Basten, M.; Blank, M;
Danly, B.G.; Guss, W.C.; Temkin, R.J.

Plasma Fusion Center
Massachusetts Institute of Technology
Cambridge, MA 02139

July 1992

This work was supported by DARPA/DSO.

Contents

List of Figures

List of Tables

Abstract

The need for radar systems with greater resolution has led to renewed interest in the development of efficient high-power amplifiers at 95 GHz. The gyro-TWT is capable of producing high power with the added attraction of having lower ohmic loading on the smooth fast-wave interaction circuit than conventional slow-wave sources. We have completed a comprehensive design of a 95 GHz gyro-TWT amplifier that is capable of producing 120 kW of output power with an efficiency of 30%, a saturated gain of 38 dB and an instantaneous bandwidth of over 5 GHz. Our concept uses an annular beam produced by a MIG electron source and operates in the $TE_{5,1}$ cylindrical waveguide mode. Realistic beam parameters from gun simulations were included in our efficiency calculations. In addition, our design includes the use of a compact superconducting magnet, quasi-optical input and output couplers and a sever to supress oscillations. The overall mechanical design shows that a compact, lightweight amplifier with adequate beam clearance is possible.

This report also includes a study of a gyro-TWT using a solid on-axis beam from a Pierce-wiggler electron source coupling with a $TE_{1,n}$ waveguide mode. Nonlinear models indicated that an efficient interaction with the waveguide mode was possible, however, beam simulations indicated that the high current density beam had large internal space charge forces that caused a substantial degradation of the beam quality.

A 95 GHz Gyro-Traveling Wave Tube Amplifier

1 Introduction

The need for radar with greater resolution, in combination with continued progress in the development of millimeter wave sources, has led to renewed interest in a high power, 95 GHz amplifier. Conventional slow wave sources, such as the coupled cavity TWT, have demonstrated peak powers up to 6-8 kW. However, large increases in power above this level are unlikely due to severe ohmic constraints. Fast wave &vices, and in particular the gyrotron, offer the best potential. The gyrotron is particularly attractive because it operates at lower voltage (< 100 kV) than other fast wave devices, such as the FEL and CARM, and the microwave circuit is simple and robust. Extensive research on high frequency gyrotron oscillators and amplifiers has demonstrated the feasibility of this approach. In this report a detailed design of a 100 kW, 95 GHz gyro-TWT amplifier will be presented.

The gyrotron is based on a resonant interaction between fast electromagnetic (EM) waves and space charge cyclotron waves on the electron beam. Because the interaction involves a fast wave, there is no need for a slow wave structure, and a smooth waveguide can be used. The elimination of this structure allows cyclotron resonance masers (CRM's) to operate at much higher powers than conventional slow wave microwave sources. The gyrotron operates with the EM wave near cutoff, and resonance is approximately given by $\omega \approx n\omega_c$, where n is the harmonic number and ω_c is the cyclotron frequency. Operating near cutoff makes the gyrotron less sensitive to beam velocity spread, which partially explains the high efficiencies that have been achieved in experiments with this device. The electrons couple to the rf electric field of a TE waveguide mode. The interaction results in a transfer of perpendicular beam energy to the rf field. Therefore it is desirable to have the perpendicular beam velocity $v_\perp$ as large as possible. As will be shown later, the need for stable operation places an upper limit on $v_\perp$ in the gyro-TWT.

A variety of experiments over the past ten years have demonstrated the viability of the gyrotron as a high power, high frequency source. Oscillators have been developed primarily as plasma heating sources for fusion experiments. The recent emphasis has been at frequencies above 100 GHz. A 140 GHz Varian gyrotron has produced 400 kW for pulse lengths up to 0.5 s. Short pulse experiments at MIT have produced powers up to 1.2 MW at 148 GHz, and step tunable operation between 120 and 327 GHz [1]. A number of gyro-TWT experiments have also been conducted. Early work included an 8.6 GHz amplifier that produced 4 MW and 16 dB of gain using an intense relativistic beam [2], and a 35 GHz experiment at NRL that operated in the TE_{01} cylindrical mode [3]. The latter device achieved gains between 20 and 30 dB,

and efficiencies up to 16%. Techniques for increasing the bandwidth by tapering the rf structure and magnetic field were also investigated [4]. A small signal gain of 18 dB was measured over a bandwidth of 12% centered at 35 GHz. A recent tapered experiment at NRL [5] has achieved small signal gains in excess of 20 dB from 27-38 GHz. A gyroklystron amplifier was also operated at NRL at 4.5 GHz [6]. Efficiencies as high as 33% were observed with a saturated output power of 52 kW. This device had a bandwidth of 0.4%. More recently gyro-TWT experiments at 35 GHz have produced 25 kW at high efficiency (23%) [7].

Varian has also been actively investigating gyro-TWT's. The initial experiments were conducted at 5 GHz [8]. The electron gun produced a 65 kV, 7 A annular beam that interacted in a circular waveguide section with the $TE_{1,1}$ mode. The rf output was extracted through a window at the end of the collector. This tube produced a peak power of 120 kW, and maximum efficiency of 26%. A small signal gain of 26 dB, and a 3 dB saturated bandwidth of 7.2% were measured. The next set of experiments were conducted at 95 GHz. Output powers in excess of 20 kW peak and saturated gains of 30 dB were obtained. The measured bandwidth was 1.5%. The peak efficiency of 8% is somewhat low, and may be due to velocity spread in the electron beam.

The goal of our study was to compare various amplifier designs and choose that device with the greatest potential to meet the performance goals. These goals are: operating frequency of 95 GHz, bandwidth of l-5 GHz, peak power of 20–100 kW, saturated gain of 30 dB, and efficiencies in excess of 20%. A duty cycle of 10% is also assumed, so the device must handle more then 2 kW of average power. In fact, the average, rather than the peak, power may be critical in determining the suitability of the source for radar applications. Simulations must indicate that these parameters can be achieved with a realistic beam with spatial and velocity spread. In order to demonstrate that gyrotrons are capable of substantial performance improvements compared to present 95 GHz sources, we have elected operating goals at the upper end of the above ranges. This leads to a technically challenging design, but we believe that the past successes of gyrotron operation in overmoded structures support its feasibility. In addition to operating goals, there are environmental constraints that must be met. These include: total system weight under 3000 lbs, operating voltage under 100 kV, power consumption must not exceed 50 kW, and adequate magnetic shielding to avoid interference with neighboring equipment.

There are also implicit constraints that must be satisfied in order to achieve successful amplifier operation. The input coupler must be able to efficiently convert the input mode (presumably the $TE_{1,1}$) into the operating mode over the bandwidth with minimal conversion into spurious modes that could oscillate or produce noise. High

efficiency is needed to reduce the power requirements of the driver. A total gain of 30 dB implies a circuit consisting of two or three sections separated by well-matched severs to avoid BW oscillations. Matching will also be critical at the input and output couplers, where reflections must be down by 20 dB. The average power requirements imply that ohmic heating losses due to the rf field must not exceed the 1 kW/cm^2 limit set by present cooling techniques. Similarly, the power density of the unspent beam in the collector must also be below 1 kW/cm^2, and there must be sufficient clearance ($\gtrsim$ 0.5 mm) between the circuit and beam to ensure robustness.

This report is organized in the following manner. A parametric study comparing various options is presented in Section 2. The best operating modes are identified and compared based on their linear gain, wall clearance, and stability. In Section 3 simulations are presented of the two guns available at MIT: a Pierce gun with a magnetic wiggler and a MIG. The information in Sections 2 and 3 was used to select the most promising design. Details of this design can be found in Section 4 including a nonlinear simulation of the interaction, a mechanical design of the overall system based on the AM1 3.4 T magnet, and analysis of critical components such as the input and output couplers.

2 Parametric Study

In order to make a proper comparison between various design options, a detailed Parametric study has been undertaken. The main purpose of this study was to determine the anticipated operating parameters and performance of each device. In addition, this study highlighted the strengths and weaknesses of each approach. The focus of this analysis was the interaction circuit. The coupling strengths and linear gain were calculated and compared to determine the most promising operating modes. The severity of mode competition was determined by identifying competing BW modes as well as their starting conditions. Other issues that were addressed include beam density and clearance. This information, in combination with the simulations of the electron guns found in Section 3, was used to select the most promising design, which was then studied in much greater detail.

The first step is selection of the beam voltage and current. Our basic design goal was an amplifier that could produce 100 kW of peak output power. This represents a substantial increase over presently available sources at 95 GHz, which can only produce up to 6-8 kW of rf power. Assuming a realistic efficiency of 25%, beam powers of 400 kW will be required. In the case of the existing Pierce gun at MIT, the inherent perveance results in operation at 74 kV and 5.5 A. More flexibility is available with the MIG. It operates with temperature-limited emission, and therefore the current can be adjusted independently of the cathode voltage by varying the cathode heater power. Although it is desirable from the standpoint of power supplies to keep the beam voltage as low as possible, the corresponding increase in current has a detrimental effect on the amplifier design. The biggest problems are the increase in the beam density, and the greater potential for exciting an absolute instability. The density increases because of the upper limit on the beam thickness imposed by the need for good coupling between the beam and rf field. The higher density leads to increased space charge forces within the beam, which enhances the velocity spread and reduces the efficiency. The limits imposed by absolute instabilites are presented below. Based on these considerations, the selected MIG parameters were 80 kV and 5 A. The gun simulations indicated a high quality beam can be produced with these parameters, and that the electric field between the anode and cathode was acceptable.

Past experiments [7] have shown that absolute instabilities can be a serious problem in gyro-TWT's. Beam parameters must be chosen carefully to avoid this instability, which can degrade or even terminate operation as an amplifier. The primary reason this instability is problematic in the gyro-TWT is the need to operate relatively close to cutoff. If the beam-wave coupling is sufficiently weak, then the beam will only

couple to the forward wave, and a convective wave grows, leading to amplification. However, if coupling is sufficiently strong, then the backward wave is excited. In this case the rf wave can grow locally from noise without propagating axially out of the system. This oscillation therefore does not require external feedback, such as reflections, to exist. In order to avoid this instability it is necessary to restrict beam parameters such as the current and a, which ultimately limits the overall efficiency.

The limits due to absolute instabilities can be obtained from the CRM linear dispersion relation, which can be written as [9]:

$$D(\hat{k},\hat{\omega}) = \left\{\hat{\omega}^2 - \hat{k}^2 - \left[1 - (1+i)\left(1 + \frac{m^2}{\nu_{mn}^2 - m^2}\hat{\omega}^2\right)\frac{\delta}{r_w}\right]\right\}(\hat{\omega} - \hat{k}\beta_{||} - nb)^2 + \varepsilon = 0. \tag{1}$$

In the above equation, the normalized frequency $\hat{\omega}$ and wave number $\hat{k}$ are given by $\hat{\omega} = \omega/\omega_{cut}$ and $\hat{k} = k_{||}/k_{\perp}$, where $k_{||}$ is the longitudinal wavenumber and $\omega_{cut} = ck_{\perp}$ is the mode cutoff frequency. The quantity $k_{\perp} = \nu_{mp}/r_w$, where ν_{mp} is the pth zero of the first derivative of the Bessel function J_m. The quantity δ is the skin depth of the waveguide wall, $\beta_{||} = v_{||}/c$, and n is the beam harmonic. The quantity $b = \omega_c/\omega_{cut}$, where $\omega_c = eB_o/\gamma_o mc$ is the relativistic electron cyclotron frequency and $\gamma_o mc^2$ is the relativistic electron energy. For a beam with all electron guiding centers located at $r = r_e$, the coupling constant ε is given by

$$\varepsilon = \frac{4\beta_{\perp}^2}{\gamma_o\beta_{||}}\frac{[J_{m\pm n}(k_{\perp}r_e)J_n'(k_{\perp}r_L)]^2}{(\nu_{mp}^2 - m^2)J_m^2(\nu_{mp})}\frac{I}{I_A} \tag{2}$$

where $\beta_{\perp} = v_{\perp}/c$, $r_L = c\beta_{\perp}/\omega_c$ is the electron Larmor radius, and the choice of signs depends on the rotation of the beam. The beam current is given by I, and $I_A = 17.045$ kA. If a lossless waveguide is assumed (Ml), then an analytic expression for the instability can be calculated [10,11] using the pinch-point theory of Briggs and Bers [12]. This expression can be written in terms of three variables: $\beta_{||}$, E, and *nb*. For now we will assume fundamental (n=1) operation. Figure 1 shows the upper limit on ε based on this formulation. Equation 2 indicates that, for a given mode, $\beta_{||}\varepsilon$ should be as large as possible in order to increase the allowable perpendicular beam energy, which scales as $\beta_{\perp}^2 I$. Figure 1 indicates that, for a given *b*, the highest values of $\beta_{||}\varepsilon$ occur at low $\beta_{||}$. This suggests that operating at high a would relax constraints due to this instability.

However, *b* and $\beta_{||}$ are actually coupled parameters if we assume operation near the "grazing" condition. In this case the electron beam interacts most effectively

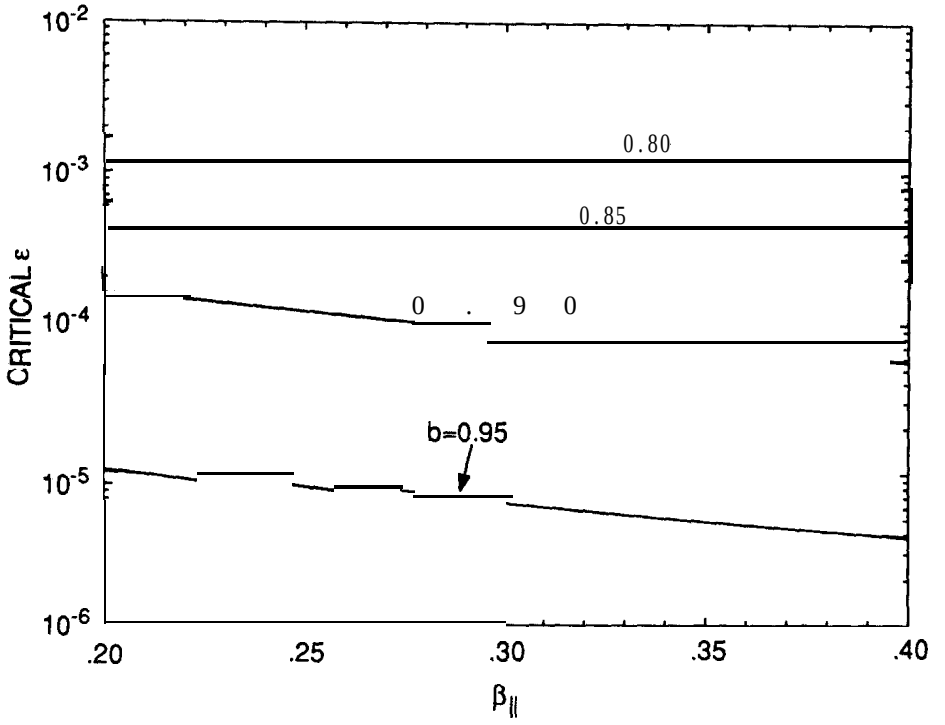

Figure 1: Upper limit on ε based on absolute instability

with the TE mode of the waveguide. This occurs when the parallel velocity of the beam is equal to the group velocity of the rf wave. This condition can be written as $b_o^2 = b^2 = 1 - \beta_{||}^2$, and results in the highest linear gain for the circuit. This equation indicates that decreasing $\beta_{||}$ increases b. One can show that this dependence leads to a reduction in the critical ε as $\beta_{||}$ decreases, and ultimately sets an upper limit on a.

The mode dependence of the critical ε can be seen in Fig. 2. The upper limit on current is shown for modes analyzed in this study. The $TE_{1,1}$ and $TE_{1,2}$ are excited by the Pierce gun operating at 74 kV, while the $TE_{4,1}$ and $TE_{5,1}$ correspond to the MIG at 80 kV. It can be seen that to avoid instability, the *a* for the $TE_{1,1}$ mode must not exceed 0.55 at 5.5 A. As the circuit becomes more overmoded, this constraint becomes more relaxed. For the $TE_{5,1}$ mode, an *a* of 0.9 is well below the instability threshold and should be acceptable. This graph was used to set *a* for the various designs.

It should be noted that Fig. 2 represents an upper limit, and that a number of factors

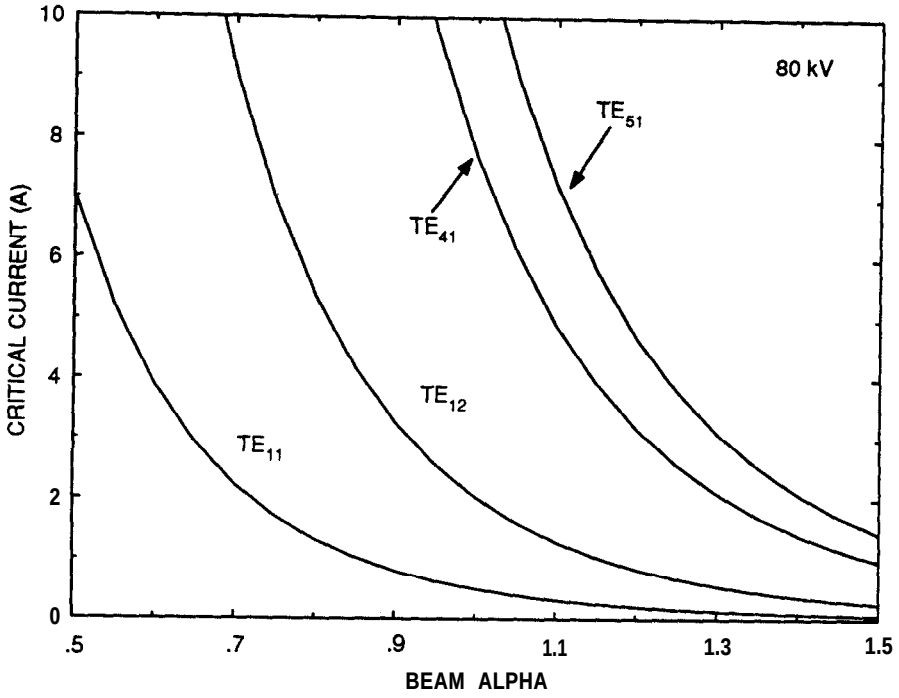

Figure 2: Upper limit on the current for the grazing condition

could increase the threshold for the absolute instability. The above analysis assumed an infinite waveguide to simplify the theory and allow an analytic solution. Inclusion of the finite circuit length would increase the instability threshold. Also, walls with infinite conductivity were assumed. Equation 1 indicates that wall resistance should be stabilizing. This is especially true for whispering gallery modes ($TE_{m,p}$ modes with $m >> p$) since their rf fields are localized near the cavity walls. Finally, it may be possible to operate below grazing ($b <$ b,), although it is likely that this will reduce the saturated efficiency.

Backward wave interactions must also be considered when evaluating the stability of the amplifier. These occur when the beam line in the dispersion diagram intersects the waveguide mode at a negative $k_{||}$. An example of this is the $TE_{2,1}$ second harmonic interaction in Fig. 3. These BW modes will disrupt the amplifier if the starting threshold is exceeded. We have calculated this threshold, using a derivation similar

to that of Park et al. [13]. This analysis assumed no energy or pitch angle spread in the beam. The nonlinear equations describing, the gyro-TWT interaction were linearized and matched to appropriate boundary conditions at each end of the circuit. This derivation is lengthy and will not be presented here. It leads to the following expression for the starting length $\hat{L}$:

$$\hat{L}^3 = \frac{2.06\beta_{||}^2\beta_{ph}^3\chi(R)}{\varepsilon(\beta_{ph}^2 - 1)^2} \tag{3}$$

where $\hat{L} = \omega L/c$, L is the interaction length, ε is defined by Eq. 2, and $\beta_{ph} = k/k_{||}$. A BW mode will be excited if $\hat{L}$ exceeds a critical value. The parameter χ depends on $R = R_1R_2$, where R_1 and R_2 are the reflections at the ends of the interaction region. When $R=0$, then χ is 7.68. For $R=0.1$, χ is 6.9, and for R=0.3, it becomes 5.4. The above equation indicates that the current needed to excite BW modes depends weakly on reflections, but strongly on L.

In the following sections specific designs will be presented based on the Pierce gun and MIG available at MIT. Basic parameters ate calulated from linear theory to determine the advantages and disadvantages of each approach. In order to provide the greatest amount of flexibility, the calculations were done with a spreadsheet (Lotus 123). This allowed us to vary circuit parameters, such as the wall radius, and quickly determine the change in operation. This information, combined with nonlinear simulations, allowed us to choose and optimize the most promising design. The details of this spreadsheet are not presented here in the interest of brevity, but it is available to the community for design purposes.

2.1 Designs Based on the Pierce Gun

These designs are based on the use of a Pierce gun combined with a magnetic wiggler to produce an on-axis beam. A beam with minimal scalloping can be injected into the wiggler and spun up with little pitch angle spread. The ability to independently control a and the cathode voltage provides operating flexibility. From the standpoint of mode interactions, the circuit can be kept small to reduce the number of modes present. If one assumes that there is no beam thickness, then ε (see Eq. 2) is nonzero, and a mode can be excited, only when m and n are equal. However, it soon becomes apparent that high current densities are needed at 95 GHz to produce 100 kW, and this can enhance the velocity spread in the beam and reduce the interaction efficiency.

B[redacted]de	n	Frequency (GHz)	Normalized Coupling $\hat{\varepsilon}$	S[redacted]rting L[redacted]ngth (cm)
For $TE_{1,1}$				
$TE_{2,1}$	2	145.8	0.64	2.2
For $TE_{1,2}$				
$TE_{1,1}$	1	61.1	4.06	5.7
$TE_{2,1}$	2	120.8	2.61	20.9
$TE_{2,2}$	2	133.8	0.82	5.5

Table 1: Strongest competing BW modes for the Pierce gun designs.

We looked at two potential modes for fundamental operation: $TE_{1,1}$ and $TE_{1,2}$. Uncoupled dispersion diagrams for these modes are shown in Fig. 3 and Fig. 4. Intersections between the beam lines, given by $\omega = n\omega_c + k_{||}v_{||}$, and mode lines, given by $\omega^2 = c(k_\perp^2 + k_{||}^2)$, were used to determine the potential resonances of these circuits. Both fundamental and second harmonic interactions were considered. The $TE_{1,1}$ has no competition from fundamental modes, but has a strong $TE_{1,2}$ second harmonic BW mode. Competition from this mode was confirmed in experiments by Barnett *et al.* [7], and high driver power (200 W) was required to suppress it. The $TE_{1,2}$ circuit has more BW resonances but they are weaker because they occur at higher $k_{||}$. Potentially the most problematic resonances are the fundamental interaction with the $TE_{1,1}$, and second harmonic coupling to the $TE_{2,p}$ modes. A thin beam should not strongly couple to the $TE_{3,p}$ modes, although the $TE_{3,1}$, with its small $k_{||}$, could be a concern. Details about these resonances can be found in Table 1. The parameter $\hat{\varepsilon}$ has been normalized to the ε of the operating mode. The starting lengths are calculated from Eq. 3 assuming a current of 5.5 A.

Design parameters for the above circuits can be found in Table 2. Operation at the grazing condition is assumed. This condition is satisfied if $\beta_{ph} = \beta_{||}^{-1}$. Once β_{ph} is fixed, then the wall radius and circuit magnetic field can be calculated. Figure 2 was used to select ***a***. The beam width was determined from the size of the beam tunnel

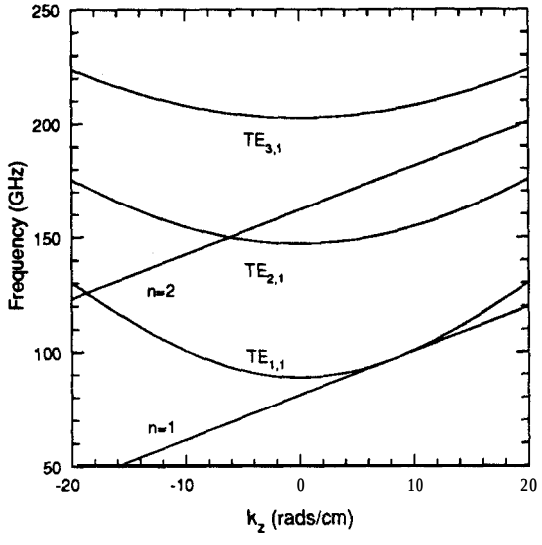

Figure 3: Uncoupled dispersion diagram for the $TE_{1,1}$ mode

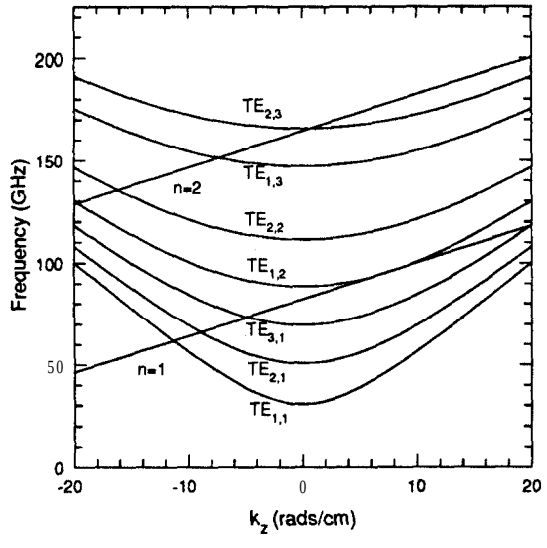

Figure 4: Uncoupled dispersion diagram for the $TE_{1,2}$ mode

Mode	$TE_{1,1}$	$TE_{1,2}$
Beam full width (cm)	0.080	0.080
Alpha	0.6	0.8
Wall radius (cm)	0.102	0.290
Beam clearance (cm)	0.047	0.233
Density (A/cm^2)	1106	1145
Space charge S	0.147	0.105
Coupling ε	5.2×10^{-5}	2.1×10^{-5}
Beam edge coupling	0.76ε	0.76ε
ν_{ph}		
Magnetic β field (T)	3.21 2.4	2.63 3.32
Linear gain (dB/cm)	9.36	7.74

Table 2: Design parameters for 95 GHz $TE_{1,p}$ amplifiers using a Pierce gun and wiggler.

in the MIT Pierce gun. The width in the tunnel was set by assuming a filling factor of 90%, and then scaled to the circuit according to the magnetic compression. Wall clearances were then calculated taking into account the Larmor radius of 0.15-0.18 mm. The strength of space charge forces in the beam are reflected in the current density and the parameter $S = 4\omega_p^2/\pi_\perp^2\bar{\omega}_c^2$, where ω_p is the plasma frequency in the beam. This parameter has been used to calculate the effect of space charge in gyrotron oscillators [14]. It can be shown that space charge enhances the bunching process but induces an energy spread which leads to a net reduction in the efficiency. This effect becomes important when $S \gtrsim 0.1$. Although S was used specifically in gyrotron oscillator theory, it is also relevant to the gyro-TWT. The other parameters in Table 2 are related to the interaction. The coupling factor ε is calculated at the beam center and at the edge. The linear gain, since it is calculated at the grazing condition, is the maximum gain [15].

Table 2 suggests that the $TE_{1,2}$ is the most promising mode for the Pierce gun. Although both modes are capable of high gain, the low a needed for stability of the $TE_{1,1}$ would ultimately limit the efficiency. An estimate of the efficiency is given by $\alpha^2\eta_\perp/(1+\alpha^2)$, where $\eta_\perp$ is the efficiency of perpendicular energy extraction. Assuming

the maximum $\eta_\perp$ of 70% [16], then the highest efficiencies possible are 18% for the $TE_{1,1}$ and 27% for the $TE_{1,2}$. The $TE_{1,2}$ mode also has more beam clearance (2.3 mm), making tube alignment less critical. Although it has more BW mode competition, the starting lengths of these modes are large (>5.5 cm).

As mentioned earlier, the biggest disadvantage of the Pierce gun design is the high current density in the beam. Densities in excess of 1 kA/cm^2 are anticipated. This is substantially higher than the 300-400 A/cm^2 typical of high frequency gyrouon oscillators. The high density was found to cause a severe degradation of the beam quality in the compression region prior to the circuit, as will be discussed in Section 3. Although we found that increasing the beam radius did alleviate this problem, a large increase is not possible because of beam interception and reduced rf coupling on the beam edge. Another disadvantage of the Pierce gun is the resulting size of the overall amplifier. A schematic of a system based on a magnet design by AM1 can be found in Fig. 5. The overall height is five feet, compared to four feet for a system based on a MIG (see Fig. 8). Substantial shielding by iron plates is needed to properly profile the field in the cathode region and provide a good match from the wiggler to the main magnet. Additional power supplies would also be needed for the wiggler and a kicker coil in the collector region. The existing Pierce-wiggler system is also quite heavy ($\approx$ 300 lbs), although a more compact Pierce gun is possible. This gun was designed to be independent of the main magnet, and therefore has substantial magnetic shielding. If the gun were designed to utilize the tail field of a particular magnet, then it is likely that the shielding and weight could be reduced. The wiggler magnets could also be incorporated into the SC magnet design.

2.2 Designs Based on the MIG

The MIG available at MIT is a compact gun capable of producing an 80 kV, 5-10 A annular beam. This gun was designed and built for $TE_{0,3,1}$ oscillator experiments at 140 GHz[17]. In those experiments up to 150 kW was generated with an efficiency of 37%, indicating the high quality of the electron beam. In Section 3 we will show that this quality is maintained when the MIG is operated at 95 GHz. In order to determine potential operating modes, one must evaluate the coupling term $J'_{m\pm n}(k_\perp r_e)$. The beam radius is determined by the cathode radius (9.12 mm) and magnetic compression. Our gun simulations showed that low velocity spreads were possible over a small range of compressions, allowing us to vary r_e somewhat in order to maximize coupling. The quality was also dependent on the magnetic gradient at the cathode. It was found that beam radii between 2.3 and 2.7 mm were possible at the circuit. The strongest

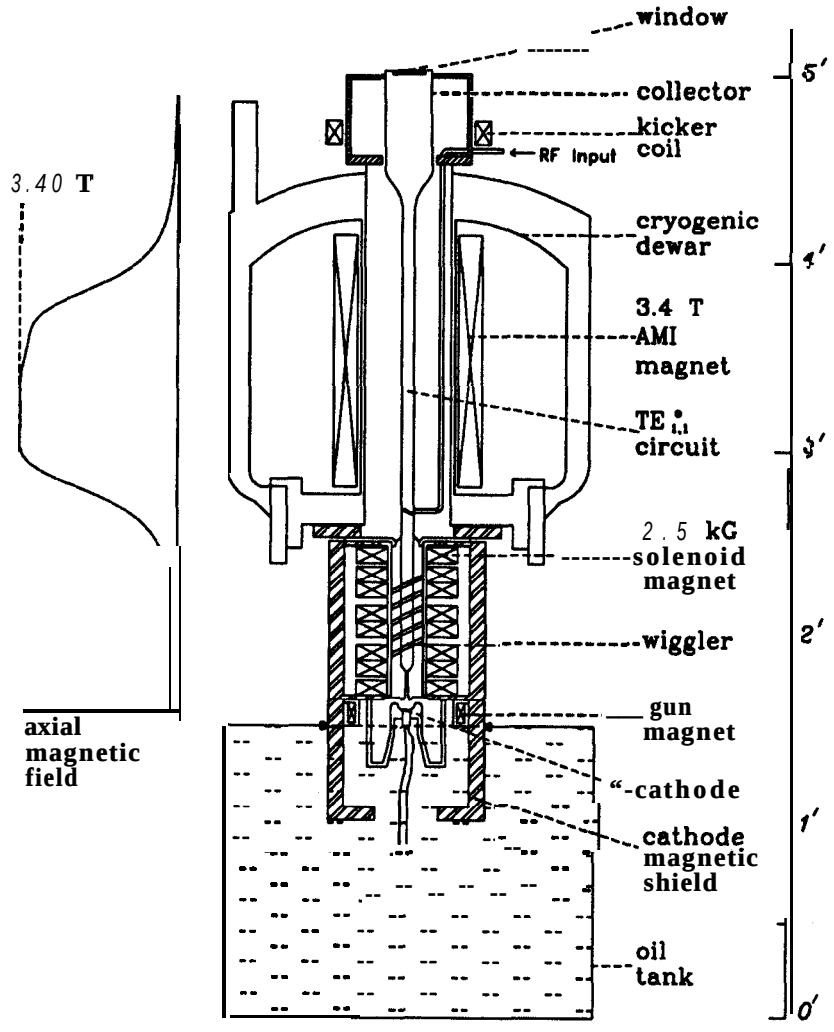

Figure 5: 95 GHz amplifier based on a Pierce gun

coupling in this case occurs for modes that satisfy $m \pm 1 = 0, 3,$ or 4. Beam clearance sets a lower limit on p. All values of p that satisfy $\nu_{mp} > k_{\perp} r_e$ are acceptable. Increasing p lowers ohmic losses but increases mode competition because of the larger circuit.

We decided to operate in whispering gallery modes with $m >> p$ in order to utilize efficient quasi-optical techniques for input and output coupling and reduce the number of competing modes. Designs based on the $TE_{4,1}$ and $TE_{5,1}$ were completed and the results are given in Table 3. The beam radii are given with their corresponding cathode magnetic fields. Higher compression is needed for the $TE_{4,1}$ to increase beam clearance. Both modes are less susceptible to absolute instabilities than in the Pierce gun case, allowing operation at higher a. Using the estimate for the efficiency described in Section 2.1, a maximum value of 32% is expected. The thin beam results

Mode	$TE_{4,1}$	$TE_{5,1}$
Beam radius (cm)	0.235 (2.2 kG)	0.263 (2.75 kG)
Beam full width (cm)	0.030	0.030
Alpha	0.9	0.9
Wall radius (cm)	0.288	0.347
Beam clearance (cm)	0.018	0.05
Density (A/cm^2)	111	98
Space charge S	0.008	0.007
Coupling ε	7.3×10^{-6}	5.0×10^{-6}
Beam edge coupling	$(0.92\text{-}1.0)\varepsilon$	$(0.87\text{-}1.08)\varepsilon$
μ_{ph}		
Magnetic β field (T)	2.68 3.38	2.68 3.38
Linear gain (dB/cm)	5.58	4.91

Table 3: Design parameters for 95 GHz $TE_{m,1}$ amplifiers

in a small variation of the coupling coefficient across the beam. The beam also has a low current density and S parameter, so space charge, effects should be minimal. The linear gain in both cases is about 5 dB/cm, suggesting a total circuit length on the order of 10 cm.

The main disadvantage of the MIG designs is the increase in competition from BW modes. This is illustrated in Figs. 6 and 7 for the $TE_{5,1}$ mode. Of particular concern are other whispering gallery modes, especially the fundamental $TE_{4,1}$ and second harmonic $TE_{10,1}$. The radial position of the beam cannot be used to selectively weaken these modes. Dispersion diagrams indicate that the same problems exist for the $TE_{4,1}$. Quantitative information about these BW resonances can be found in Table 4. Both modes have similar characteristics, with fundamental BW competition at about 70 GHz, and second harmonic at about 160 GHz. The minimum starting length is about 2 cm in both cases. This indicates that severs will be required to reduce the interaction length available for BW oscillations. Note that the easiest BW modes to excite do not necessarily have the strongest coupling. Excitation has a much stronger dependence on the resonance $k_{||}$, so techniques that selectively increase the $k_{||}$ of these modes could effectively suppress them. This will be further discussed in Section 4.

Because of the similar operating characteristics of the two MIG designs, the $TE_{5,1}$ is preferable for greater beam clearance.

BW Mode	n	Frequency (GHz)	Normalized Coupling	Starting Length (cm)
For $TE_{4,1}$				
$TE_{2,1}$	1	66.0	2.07	4.61
$TE_{3,1}$	1	73.3	1.40	2.79
$TE_{4,2}$	2	155.4	0.25	3.65
$TE_{8,1}$	2	160.2	0.41	2.14
For $TE_{5,1}$				
$TE_{4,1}$	1	75.2	1.47	2.69
$TE_{1,2}$	1	75.3	0.60	3.60
$TE_{6,2}$	2	161.3	0.23	2.50
$TE_{10,1}$	2	161.8	0.39	1.94

Table 4: Strongest competing BW modes for the MIG designs

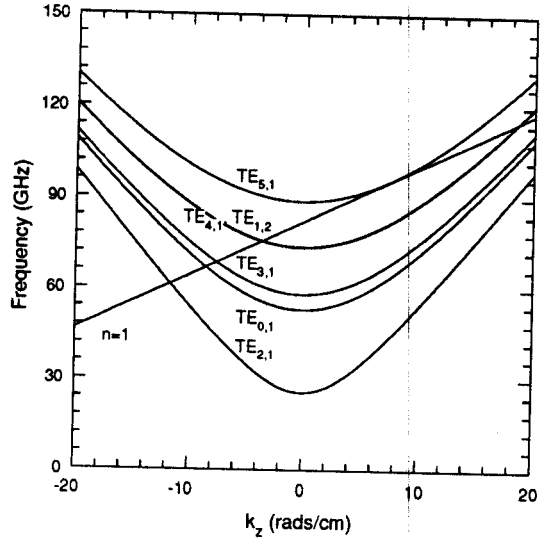

Figure 6: Fundamental dispersion diagram for the $TE_{5,1}$ mode

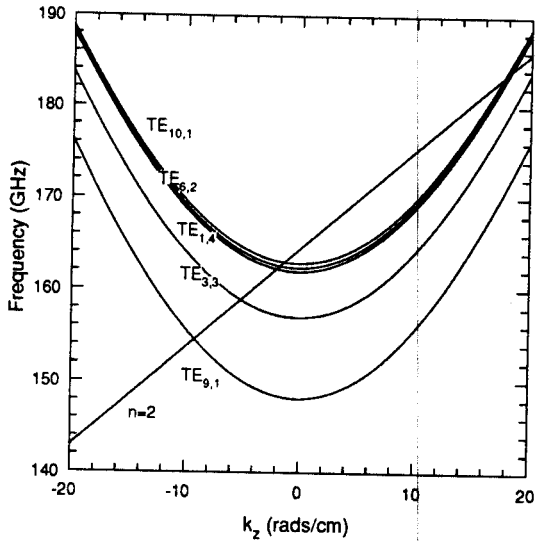

Figure 7: Second harmonic dispersion diagram for the $TE_{5,1}$ mode

2.3 Design Selection

Based on this parametric analysis we have selected the $TE_{5,1}$ MIG design. The Pierce gun designs are attractive because of fewer competing modes, but we felt space charge effects would be too severe. It is possible to enlarge the beam and reduce these forces by changing the magnetic flux through the cathode, but this would increase beam scalloping and interception. In addition coupling at the beam edge would be low, reducing the efficiency. A Pierce gun designed to produce peak rf powers of 20 kW with an 80 kV, 1 A beam would have an acceptable current density, but the low output power is unattractive. Our calculations also show that α would be restricted to low values (0.5–0.8) for the $TE_{1,1}$ and $TE_{1,2}$ modes, and that a higher α would require operation in a higher order mode with greater mode competiiton.

The total $TE_{5,1}$ amplifier system is quite attractive. A final mechanical design using the AMI magnet was completed, and a schematic can be seen in Fig. 8. The overall system is under four feet in height and meets the weight specifications. The four inch warm bore provides sufficient room for the circuit and input coupler. A small trim coil may be needed to adjust the field gradient at the cathode to optimize the beam quality. The MIG produces a high quality beam that is capable of generating high efficiencies. The input coupler consists of an inverse Vlasov launcher and mirror illuminated by a horn propagating the $TE_{1,1}$ mode. The coupler is compact and easily fits between the gun and circuit. The guide for the input power would be low loss corrugated waveguide. The ouput coupler is also based on the Vlasov coupler, but must be somewhat larger to accomodate the high output powers and provide clearance for the beam. The collector is a separate component, and could be depressed to increase the efficiency. More discussion of the individual components can be found in Section 4.2. The challenges will be in the design of a stable circuit. It should be noted, however, that the BW competition in the $TE_{5,1}$ design is comparable to that in the $TE_{1,1}$ Pierce gun design. Such competition has been effectively reduced with a sever in $TE_{1,1}$ experiments at 35 GHz [18].

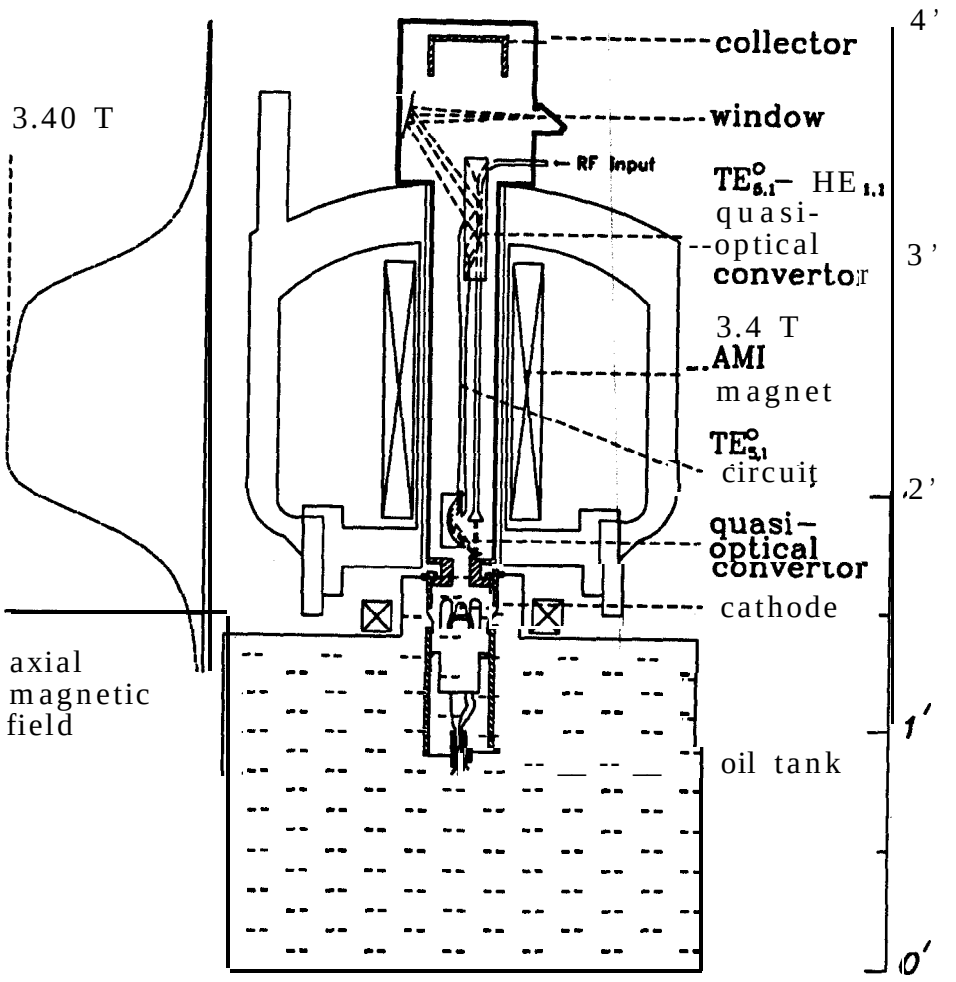

Figure 8: 95 GHz amplifier based on a MIG

3 Modeling of Electron Guns

Efficient coupling to the rf circuit in the gyro-amplifier requires a high-quality electron beam placed at the appropriate radial position in the interaction waveguide. A detailed study of both a Pierce-wiggler and a MIG beam forming system was completed. Both systems were based on existing equipment at MIT. In order to realistically estimate the quality of the electron beams, 2D and 3D electrostatic trajectory codes were used. The use of these codes allowed for the self-consistent calculation of the average perpendicular and parallel velocity, beam radius and thickness, and the spread of the electron velocity distribution. These codes were used to model the beam as it is magnetically compressed up to the interaction region.

After the evaluation of both the Pierce-wiggler and MIG beam forming systems it was decided that the MIG would better satisfy the constraints of the 95 GHz amplifier design. The MIG delivered a higher quality beam to the interaction region with transverse velocity spreads of less than 5% at 5 A and 80 kV. In contrast, the Pierce-wiggler system had spreads in excess of 15% in nearly all cases due to the large current densities in the beam as it was compressed into the interaction region. Since the MIG operates in the fringe field of the interaction magnet, it is a lighter and more compact electron source and lacks the added complexity of a wiggler, wiggler-solenoid, and the magnetic shielding of the Pierce-wiggler system. Although there may be ways to tailor the wiggler profile to reduce this spread, it was felt that this would lead to an even larger gun system. Selection of the MIG resulted in the choice of the $TE_{5,1}$ mode for the primary design. Details of the gun simulations are given in the following sections.

3.1 Pierce Gun

A Pierce diode source with a bifilar helical wiggler was first examined. Such a configuration would provide an on-axis solid beam which could be used to couple into a $TE^{\circ}_{1,n}$ waveguide mode. An existing system at MIT was used as the basis for this design study and is shown in Fig. 9. This Pierce-wiggler beam system is capable of producing 6.1 A of beam current at an energy of 80 keV. The cathode emission is space-charge limited with a measured micro-perveance of 0.27. The beam is matched into an axial magnetic field generated by a solenoid assembly that is mounted to the gun assembly. This solenoid is formed by four separate 'pancake' coils that can be independently controlled for field profiling. A flat-field region of 6 inches at 2.5 kG is possible. A permanent magnet bifilar helical wiggler is used to give the electrons

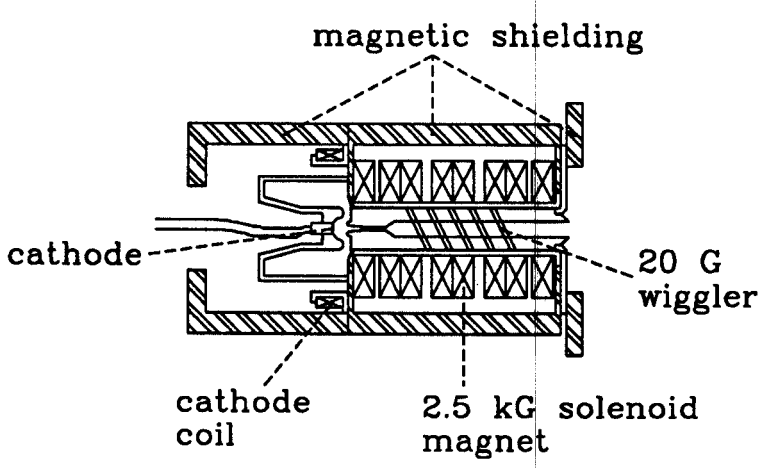

Figure 9: The Pierce-wiggler beam system.

a small perpendicular velocity component ($\beta_\perp$) in the solenoid guide field. Magnetic compression serves to increase $\beta_\perp$ to the value desired in the interaction circuit. This wiggler provides a ≈20 gauss transverse magnetic field and it can be re-wrapped *in situ* if changes in pitch or transverse field strength are necessary. An additional coil is placed around the cathode for independent adjustment of the magnetic flux at the cathode surface. In such a beam producing system, stray magnetic fields can have a deleterious effect on cathode and wiggler performance. Magnetic shielding in the form of steel shells around the cathode and solenoid and a large steel washer between the solenoid and interaction magnets serve to limit the amount of stray flux from the interaction magnet. Stray cathode flux from the solenoid magnet is limited by a thin plate between the gun and solenoid assemblies. The result is a compact, although somewhat heavy (≈300 lbs.), electron beam forming system that can be matched to a wide range of interaction magnetic fields.

The two-dimensional electron beam optics code EGUN was used to model the electrons in the cathode-anode region for a range of beam voltages and cathode magnetic fields. A typical set of EGUN trajectories is shown in Fig. 10. These trajectories were calculated with a anode voltage of 70 kV, beam current of 6.1 A, and a solenoid guide field of 2.5 kG. The Brillouin parameter ($m = \omega_c^2/2\omega_p^2$) is 2.9 and beam scallop is 4.0%.

The magnetic circuit of the Pierce-wiggler beam system, and in particular, the matching between the solenoid and interaction magnet was modeled with the magnet code Poisson. An example of the calculated field along the axis is shown in Fig. 11.

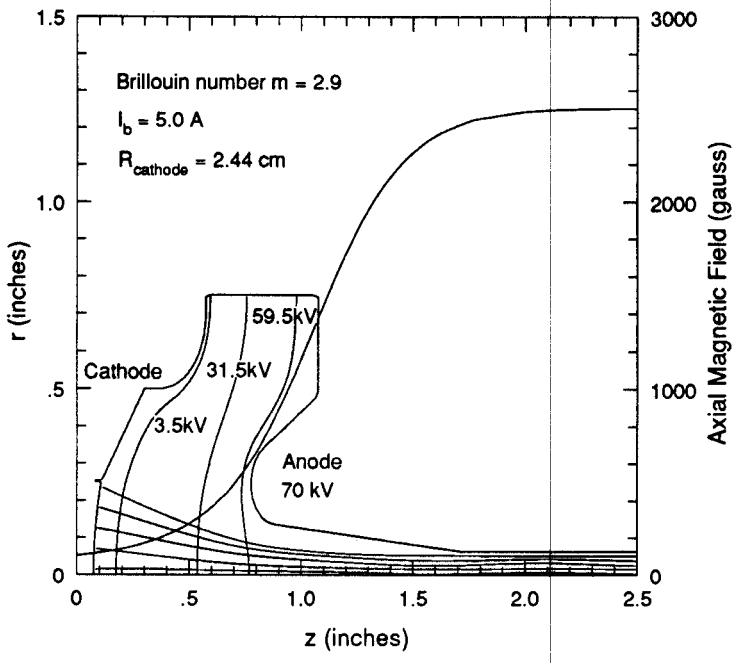

Figure 10: EGUN trajectories for the Pierce gun. Note only 5 trajectories are shown, although up to 20 have been used with no appreciable change in the results.

Exact dimensions of the various components in the magnetic circuit of the Pierce-wiggler were obtained and all shielding pieces were modeled as 1020 steel. The plate between the gun assembly and solenoid assembly is actually made out of a material called 'Vatmelt' and thus the fields near the cathode may be slightly different. It should also be pointed out in Fig. 11 that the interaction magnet coil set was modeled on an existing magnet and not the AMI magnet design. The magnet used here has a longer ramp but it was demonstrated that, in principle, a smooth transition could be obtained between the Pierce-wiggler and a 3.4 T interaction magnet.

After the electron beam exits the cathode-anode area it has only a very small transverse velocity due to its Pierce rotation. The beam is given more $\beta_\perp$ in the wiggler and then $\beta_\perp$ is increased adiabatically as the magnetic field increases to the interaction region. At the wiggler entrance the initially on-axis beam is kicked off-axis and an azimuthally asymmetric situation is created. Hence, codes that assume azimuthal symmetry, such as EGUN, can no longer be used. A three dimensional trajectory code TRAJ was developed at MIT explicitly for the case of a solid beam

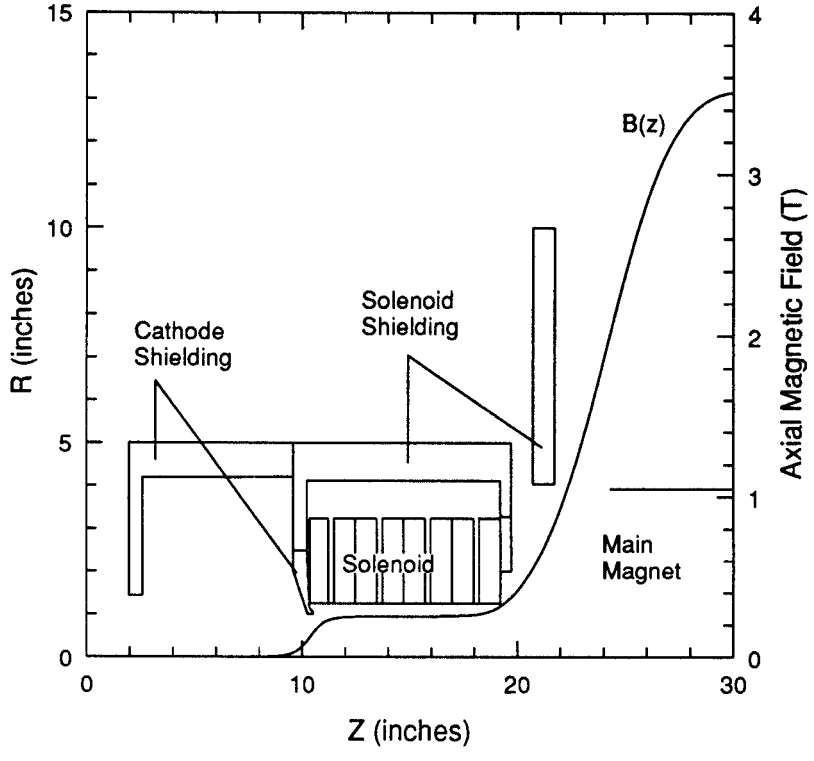

Figure 11: Calculated axial magnetic field of the Pierce-wiggler beam system and layout of the model used in Poisson.

spiraling down the drift tube due to the effects of a wiggler. TRAJ includes the self-consistent effects of radial and azimuthal electric fields and self-B_θ fields, but not the effects of self-B_r or self-E_z fields. Self-fields are obtained by solving Poisson's equation on a polar grid in a fixed z-plane as the particles move along the axis. TRAJ allows for an extra set of coils so that realistic beam parameters can be obtained in the magnetic compression region.

The wiggler is modeled in one of three ways: as a 'perfect' wiggler with no variation of the transverse magnetic field with radius, as a wiggler with variations in field given by an n^{th} order modified Bessel expansion, or, by computing the full Biot-Savart fields by breaking each wiggler current loop into a finite number of small,

straight segments of current. Obviously, the last method is the most numerically intensive. In our case the beam radius was much smaller than the wiggler helix radius ($R_b/R_w \approx 0.1$) and our situation was modeled reasonably well using the first method. Typically, the full-blown wiggler field calculations were used as a check on wiggler end-effects at the entrance and exit. Adiabatic wigglers can also be modeled by tapering the transverse fields at the entrance.

Two methods of initial beam loading were used. The first method initializes the electron velocity, energy, current per ray, and position according to the output from an EGUN simulation. The current rays are then copied azimuthally and the simulation begins. The other method loads the particles with a specified energy, velocity, and maximum beam radius and assigns rotational velocity according to a rigid-rotor model of the beam. Both methods gave similar results for the same beam parameters, although the first method has an intrinsic 'graininess' due to the finite number of rays used in EGUN.

Figure 12 demonstrates the sequence of the initial loading of a rigid-rotor beam with 512 particles and the magnetic compression of the beam. Also shown are the average α and the relative transverse momentum spread as a function of length. This case is for a 60 kV, 4 A beam with an initial radius of 1.32 mm. The beam travels through a 15 gauss wiggler which has a length of $3\lambda_w$, where the wiggler pitch, λ_w, is 2.38 cm. At the wiggler entrance the beam has a natural momentum spread due to the Pierce rotation of the beam. The relative spread in $p_\perp$ decreases dramatically as the beam is acted on by the wiggler if the Brillouin number is sufficiently large. As seen in Fig. 12, the beam has been kicked off-axis by the wiggler and the beam center rotates about the axis at ω_c.

As the beam travels into the high field of the interaction magnet the average α increases and the relative spread in $p_\perp$ increases because the helical motion of the beam has caused large asymmetric space-charge forces. This is a consequence of the relatively large current density in the beam ($\approx 800 A/cm^2$) and requires a detailed look at the trajectories of individual particles for understanding. Shown in Fig. 13 are the actual paths of the beam center and an electron over one cyclotron wavelength. The beam 'wobbles' around the axis at ω_c and the electron has an orbit that takes it from the beam center to the edge of the beam, and then back to the beam center. The radial electric field that the particle sees varies from -1 kV/cm near the center to -12 kV/cm at the beam edge. The particle is accelerated while moving from position 1 to 7 in Fig. 13 and decelerated on the way to position 10, but, since the particle is now relatively closer to the beam center, it is decelerated by a smaller E_r. The result is an net increase in the $p_\perp$ of the particle at the end of the orbit. The calculated

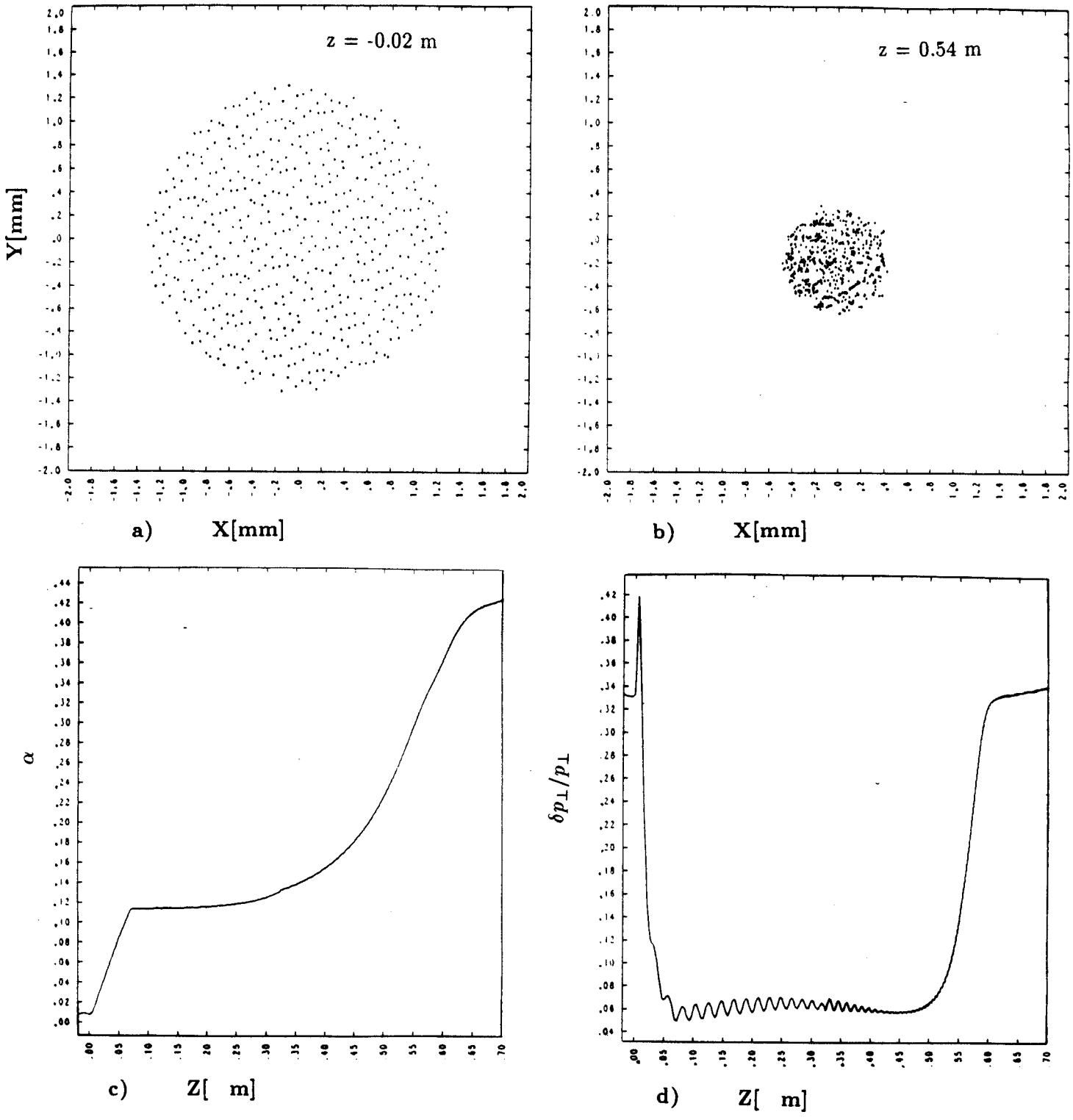

Figure 12: TRAJ simulation for a beam with energy of 60 keV, a current of 4 A, and an initial radius of 1.32 mm. Plots a) and b) show the initial loading and the compression of the off-axis beam. The average α and relative spread in the transverse momentum are shown in c) and d). The wiggler extends from 0.0 to 0.0714 and has a transverse field of 15 gauss.

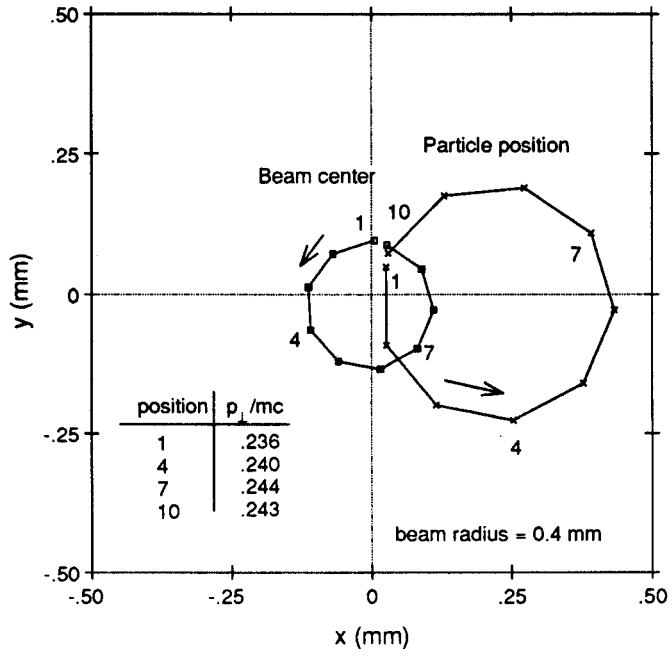

Figure 13: Beam center position and particle position for a single orbit in the compression region. The self-electric field at the particle position is essentially radial from the beam center position.

values of $p_\perp$ at position 1,4,7 and 10 are given in the table in Fig. 13. Particles that are phased behind the beam center will lose $p_\perp$, while particles that move exactly in phase with the beam center will have no net change in $p_\perp$ over a cyclotron orbit. Accumulating over succesive cyclotron orbits, the induced spreads can increase rapidly in the compression region as evidenced in Fig. 12. This process continues with each successive cyclotron orbit until the particle motion is no longer correlated with the beam center motion, or, in other words, until the beam diffuses azimuthally around the axis.

Clearly, a beam with large tranverse momentum spreads is not desirable. In the case of the existing Pierce-wiggler system, the maximum beam radius at the wiggler entrance is constrained by the size of the anode aperture at the gun exit. A transverse momentum spread of 18% for an α of 0.5 at the interaction region was obtained by increasing the beam size at the wiggler entrance to its maximum value. This represents the best case for the existing gun.

Methods for obtaining low velocity spreads from high current density Pierce-

wiggler sources may exist. Ginzburg [19] recently proposed an approach that involves tailoring both the wiggler transverse field and the solenoid guide field to produce a beam that is essentially 'mixed' at the wiggler exit. This method was considered but because of the added length and complexity it was dropped in favor of a MIG design. It should be noted that this problem is less important in highly relativistic devices such as the CARM because space charge forces are small.

3.2 Magnetron Injection Gun

Due to the poor beam quality and the large size and weight of the Pierce-wiggler system, a design based on a magnetron injection gun (MIG) was examined. As with the Pierce gun, the MIG design is based on an existing gun at MIT. This gun was used with good results on several gyrotron oscillator experiments. The MIG produces an annular beam with much lower current densities ($\approx 100 A/cm^2$) than the Pierce gun and lower transverse spreads ($\leq 5\%$) are possible. A schematic of the MIG is shown in Fig. 14. An electric field normal to the emitter surface is generated by the gun anode and electrons are pulled off the emitter and then accelerated down the drift tube by the main anode. Since the MIG operates in the fringe field of the interaction magnet and $\beta_\perp$ is imparted through the gun anode rather than a wiggler system, the MIG presents a beam forming system that is about half the length, half the diameter, and less than one-fifth of the overall weight of the Pierce-wiggler system.

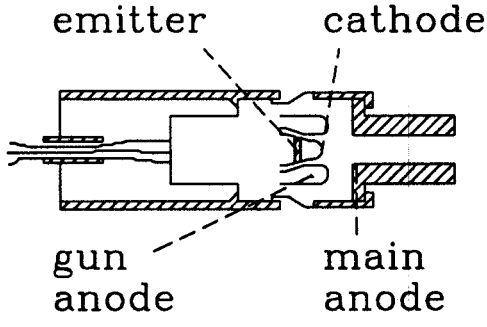

Figure 14: Schematic of the 80 kV, 5 A magnetron injection gun

In order to evaluate MIG performance and beam characteristics at the circuit, the

electrostatic two-dimensional code EGUN was used. Two interaction magnetic field profiles were used in the simulations and these are compared in Fig. 15. The first profile included field shaping in the gun region in order to decrease the magnetic field gradient at the cathode. The second design did not include any shaping at the cathode, with larger field gradients as a result. At the emitter the gradients were 96 and 320 gauss/cm, respectively. In general, the simulation of the MIG in either field profile predicted a high-quality beam ($\delta\beta_\perp/\beta_\perp \approx .05$) at the circuit, provided that the MIG was operated at a lower compression ratio (higher cathode magnetic field) with the second magnet design. The second AMI design was chosen because a larger beam was desirable for the $TE_{5,1}$ mode and the magnet design without field shaping was shorter.

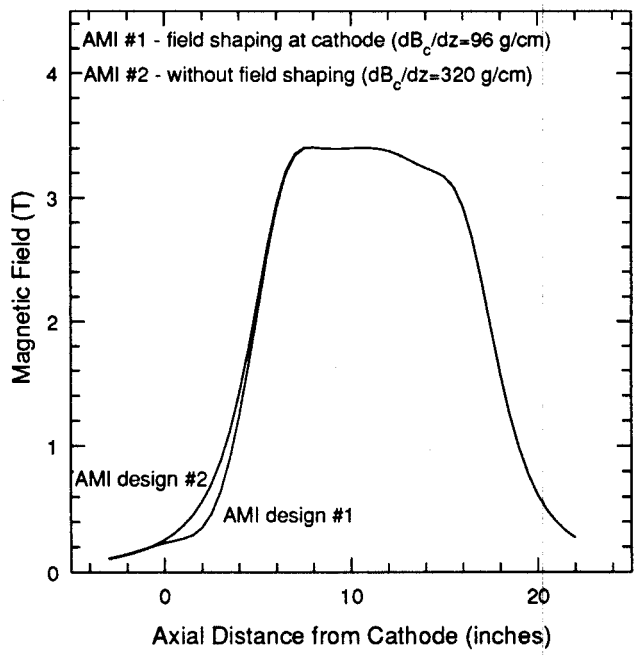

Figure 15: Comparison of both superconducting magnet designs. The first design includes field shaping in the cathode region.

An example of the electron ray trajectories calculated by EGUN is shown in Fig. 16. For a magnetic compression ratio of 13.1 the beam at the circuit has an α of

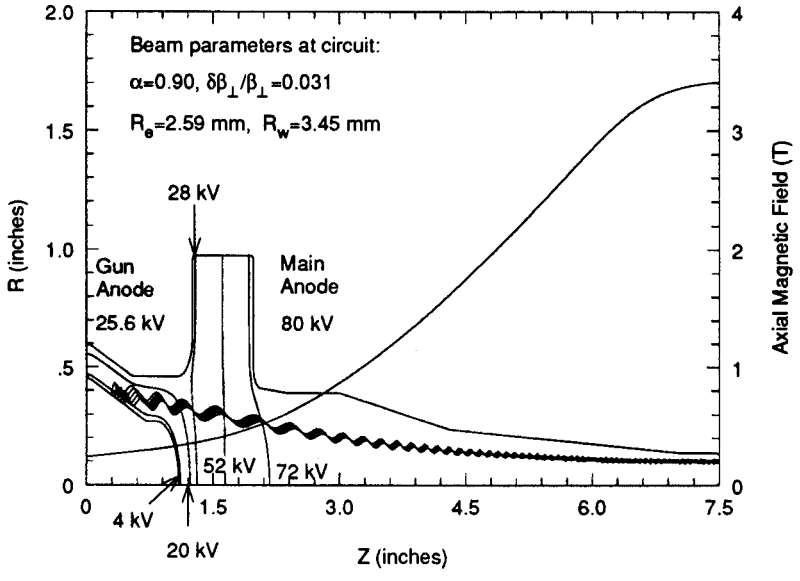

Figure 16: Ray trajectories from EGUN. Note only five rays are plotted here, although up to 80 rays have been simulated with no appreciable change in the results.

0.9 with a transverse spread in $\beta_\perp$ of 3.1%. Fig. 17 shows the predicted α and $\delta\beta_\perp/\beta_\perp$ at the circuit as a function of the gun anode voltage. The current density of the beam from the MIG source is much less than that of the beam from the Pierce-wiggler design and significantly lower spreads are possible. As the α is varied over the range from 0.80 to 0.93 only a slight increase in $\delta\beta_\perp/\beta_\perp$ is expected. Unlike the Pierce gun, beam current can be varied independently of the cathode voltage, and Fig. 18 summarizes the expected $\delta\beta_\perp/\beta_\perp$ for a range of beam currents. The transverse spread increases with current density but is predicted to be less than 5% even at 7.5 A of beam current.

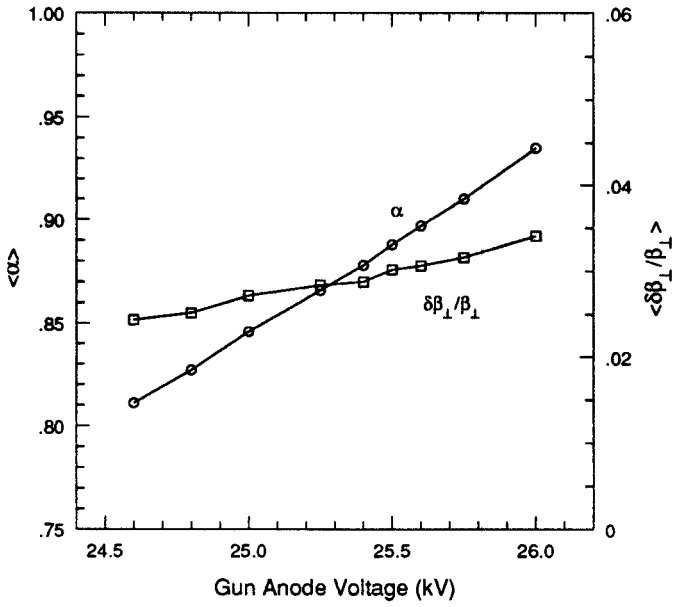

Figure 17: Predicted α and $\delta\beta_\perp/\beta_\perp$ at the interaction region as the gun anode voltage is varied. The beam voltage and current are 80 kV and 5 A.

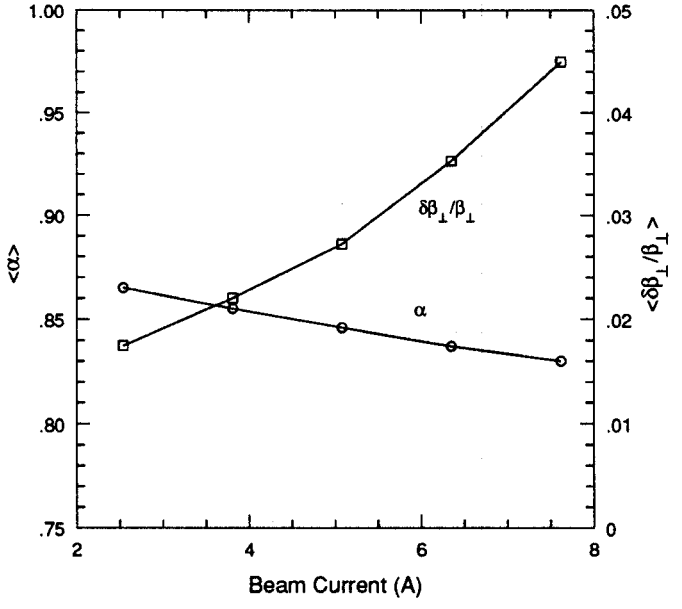

Figure 18: Predicted α and $\delta\beta_\perp/\beta_\perp$ at the interaction region as the beam current is increased for a 80 kV beam. Note spreads of less than 5% are expected over a wide range of beam current.

4 Gyro-TWT Amplifier Design

We have selected the $TE_{5,1}$ fundamental gyro-TWT as our primary design. It is based on the high quality beam produced by a MIG and provides adequate beam clearance, good coupling to the rf field, and high linear gain. In this section the nonlinear behavior of this design is presented, including the saturated output parameters and bandwidth. Tapering of the magnetic field was investigated and found to increase the efficiency from 17% to 31% without degradation of the bandwidth. Details about individual components of the circuit are also presented.

4.1 Simulations

Nonlinear simulations of the amplifier were carried out with the MIT slow-time-scale gyrotron/CARM amplifier code SPOT [20]. This code employs the slow-time-scale self-consistent single particle equations of motion together with the wave equation to calculate the nonlinear saturation of cyclotron-resonance amplifiers, including the effects of beam spread in guiding center, energy, and parallel momentum. A magnetic field tapering is incorporated into the code for efficiency enhancement schemes. This code has been successfully benchmarked against PIC codes (MAGIC and UCLA PIC codes) and against the amplifier code of A. Ganguly at NRL [21]. It has also been checked in the small signal regime with the growth rate predicted by the linear dispersion relation. Figure 19 shows such a comparision. The output power as a function of interaction length has been calculated for the $TE_{4,1}$ mode at 95 GHz based on an 80 kV, 6 A beam. There is good agreement of the predicted gain in the linear region (about 6.5 dB/cm). Similar results can be obtained for the $TE_{5,1}$ mode.

The coupled dispersion relation is useful in determining the coupling strength, growth rate, and bandwidth of the desired and competing modes. This relation is given by Eq. 1, with ε given by Eq. 2. Fig. 20 shows the dependence of ε on the beam radius for the $TE_{5,1}$ circuit. The coupling strength in this figure is given by $J^2_{m-1}(k_\perp r_e)/(\nu^2_{mp} - m^2)/J^2_m(\nu_{mp})$. For our design the beam is located at r_e/r_w=0.76, which is close to the maximum coupling. The beam is slightly inside the peak to increase the beam clearance. Figure 21 shows the dependence of the linear growth rate on frequency. High gain (5 dB/cm) is predicted from 90 to 97 GHz, which is greater than the 5 GHz bandwidth specified.

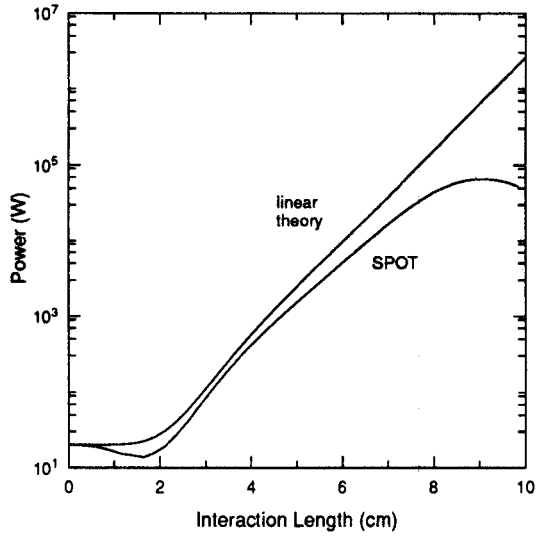

Figure 19: Comparison of linear theory and SPOT nonlinear code

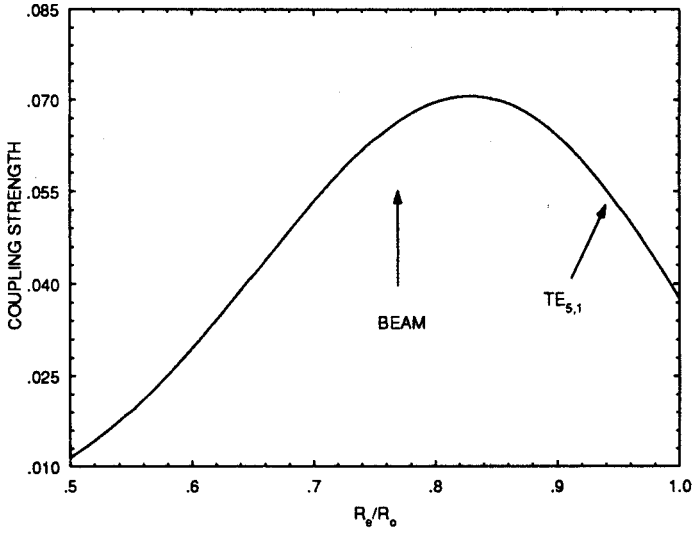

Figure 20: Beam coupling vs beam radius

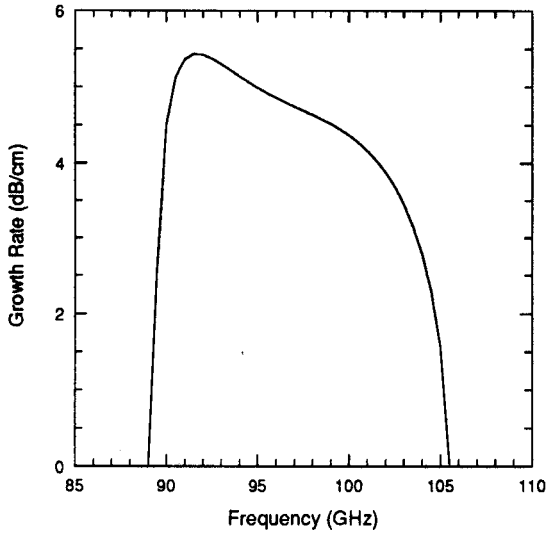

Figure 21: Linear growth rate for $TE_{5,1}$ mode

We have also calculated the gain of competing modes over this range, and found that the maximum forward amplification was 1.8 dB/cm for the $TE_{4,1}$ mode. This lower gain, in combination with an efficient $TE_{5,1}$ input coupler, should prevent the $TE_{4,1}$ mode from growing to a large signal.

In our nonlinear simulations both uniform and tapered magnetic fields in the circuit region were investigated. The final design results are shown in Table 5. In all cases the input power was 20 W. We have assumed a perpendicular velocity spread of $\pm 5\%$ and a beam thickness of 0.3 mm, which is consistent with our EGUN simulations. The large β_{ph} of these designs suggests that they should be somewhat insensitive to velocity spread. We found that the efficiency only decreases modestly until the velocity spread exceeds 5%. The table shows that, in spite of the low α, high efficiency is possible. This is especially true for the tapered field results. The modest tapering required can be achieved with SC magnets, as the AMI magnet design demonstrates. Both designs provide saturated gains well above the 30 dB required. The saturation lengths are short and help to keep the overall system compact. For comparision purposes, $TE_{4,1}$ mode designs were also completed and can be found in Table 6. As expected, the operating characteristics of this mode are very similar to those of the $TE_{5,1}$.

For the uniform magnetic field case, the design was optimized by varying the field

Magnetic Profile	Flat	Taper
Current(A)	5.0	5.0
Voltage(kV)	80	80.
Velocity ratio	0.9	0.9
Beam radius(cm)	0.263	0.263
Waveguide radius(cm)	0.345	0.345
$k/k_{\|\|}$	2.79	2.8
Δ	0.25	Varies
Magnetic Field(T)	3.35	3.40–3.16
Output Power(kW)	85.8	123.4
$\eta_T(\%)$	17.4	30.7
Saturated gain(dB)	36.3	37.9
Saturation length(cm)	14.1	19.5

Table 5: Design Parameters for $TE_{5,1}$ mode

until the power was maximized. The sensitivity of the output power to this variation is shown Fig. 22. The detuning parameter is defined as:

$$\Delta = \frac{2(1-\beta_{\|}/\beta_{ph})}{\beta_{\perp}^2(1-\beta_{ph}^{-2})}\left[1-\frac{\beta_{\|}}{\beta_{ph}}-b(1-\beta_{ph}^{-2})^{0.5}\right] \tag{4}$$

where $b=\omega_c/ck_{\perp}$. Values of Δ between 0.2 and 0.3 produce high powers, although it may be preferable to operate at the lower end of this range to reduce the saturation length. It was also found that the power can be increased without hurting the efficiency by increasing the beam current. Figure 23 shows the evolution of rf power as a function of axial length for the design parameters in Table 5. The output power increases at about 3.1 dB/cm, and saturates in 14 cm with an output power of 86 kW. Longer interaction lengths result in reabsorption by the beam as the electron bunch oscillates in the bucket.

It is well known that tapering the magnetic field allows the electrons to remain in resonance longer with the rf field as they lose energy, and thus leads to higher

Magnetic Profile	Flat	Taper
Current(A)	6.2	6.2
Voltage(kV)	80	80.
Velocity ratio	0.9	0.9
Beam radius(cm)	0.237	0.237
Waveguide radius(cm)	0.286	0.286
$k/k_{\|\|}$	2.79	2.79
Δ	0.26	Varies
Magnetic Field(T)	3.34	3.4–3.2
Output Power(kW)	101	160
$\eta_T(\%)$	20.4	32.3
Saturated gain(dB)	36.9	39.0
Saturation length(cm)	12.2	16.2

Table 6: Design Parameters for $TE_{4,1}$ mode

efficiency. A variety of linear tapers was studied, and the best profile was found to be an initial uniform field while the electrons bunch followed by a negative linear taper. In order to form the bunch as quickly as possible, the magnitude of the uniform field (3.4 T) was chosen such that the linear gain was as high as possible (ie., Δ = 0). The negative taper was then started as the efficiency begins to saturate and the electrons began to reabsorb energy. For the $TE_{5,1}$ design this occured after 11 cm. The dependence of the output power and efficiency on the taper gradient can be seen in Fig. 24. In all cases the interaction length was between 19 and 20 cm. Higher powers were possible with low gradients and very long interaction lengths (30–40 cm), but these were not considered realistic designs. When the gradients become too large, then some electrons are not trapped in the bucket and their energy is lost, leading to lower efficiencies. The optimum design has a taper of -0.7%/cm over 8.5 cm, for a total drop of 6%. The power variation versus distance is shown in Fig. 25 for 20 W of input power. One concern about using a magnetic taper is a possible reduction in the bandwidth. We investigated this with SPOT by running simulations for different frequencies and interaction lengths, with the results shown in Fig. 25. The best length

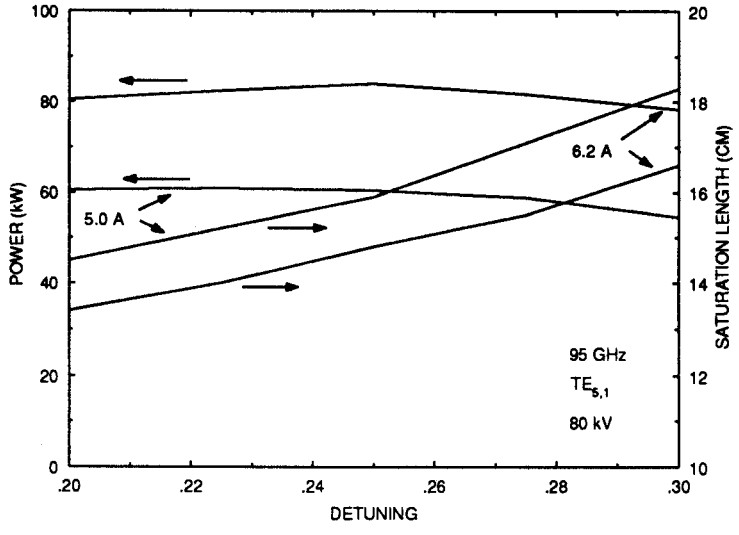

Figure 22: Optimization of uniform field design

is 19.5 cm, with powers between 100 and 125 kW over a 5 GHz range. This satisfies the design specifications.

4.2 Mechanical Design

In order to determine the overall system layout, we completed a mechanical drawing of the $TE_{5,1}$ amplifier. This was discussed earlier in conjunction with Fig. 8. The magnet is based on the magnetic profile needed to achieve a high quality beam, and high efficiency in the circuit. The warm bore dimensions were chosen to allow passage of the tube. This information was sent to American Magnetics, Inc. (AMI), who produced a design of the coil set and cryostat with assistance from Cryogenic Technical Services (CTI). System constraints such as size, weight, cost of operation, helium hold time, and required electronics were considered. Two iterations produced a compact, 3.4 T magnet one meter high with a vertical bore. This magnet has sufficient helium for one week. Further refinements may lead to an even smaller system.

Two magnets were designed based on the field gradient at the gun cathode and their magnetic profiles are compared in Fig 15. The first design included field shaping at the cathode to decrease the field gradient to 150 gauss/cm while the second design

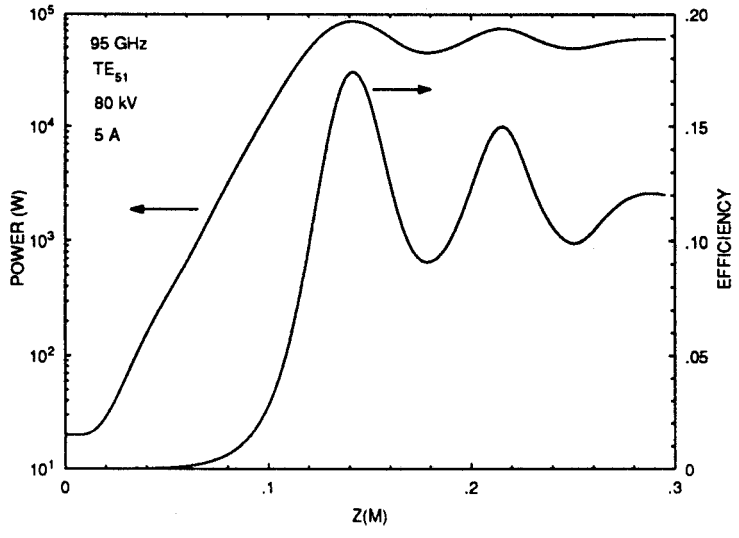

Figure 23: Power and η versus length for uniform magnetic field

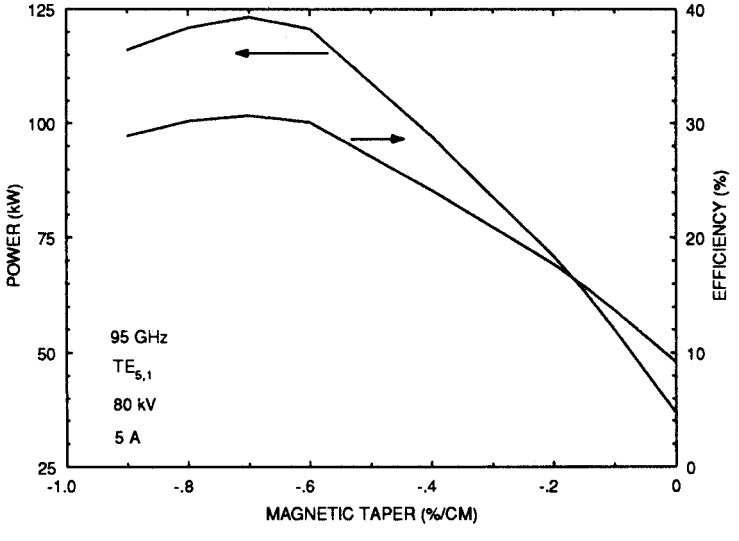

Figure 24: Optimization of tapered design

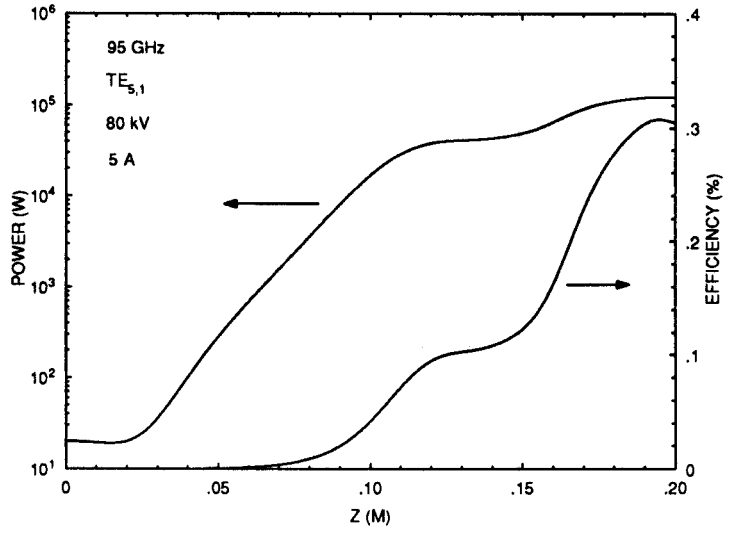

Figure 25: Power and η versus length for tapered magnetic field

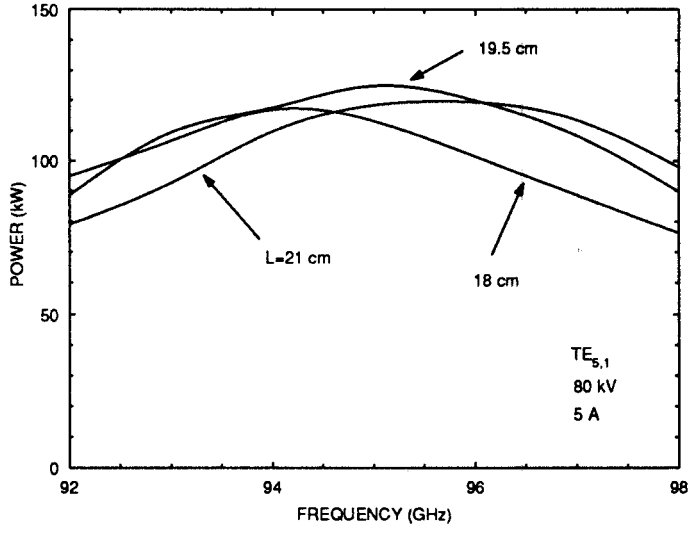

Figure 26: Bandwidth of tapered $TE_{5,1}$ design

did not include field shaping and had a gradient of 320 gauss/cm at the cathode. As discussed in Sec. 3 the MIG gun operated well in the fringe field of the second magnet provided that the gun was operated at a lower magnetic compression ratio. Since a larger beam was desired for the $TE_{5,1}$ circuit, and because the magnet was slightly smaller and lighter, the second magnet design was chosen for the gyro-TWT. The magnet has a vertical design with a high-field region 8.0 inches in length with a linear downtaper for increased amplifier efficiency over the last 4.0 inches. The MIG gun will be mounted with the cathode only 7.0 inches from the beginning of the high field region.

The size and weight of the magnet make it very attractive for an airborne gyro-TWT. Total weight of the magnet and dewar was estimated to be less than 130 lbs. and the overall height and diameter are only 30 and 20 inches, respectively. The reduction in size is partially at the expense of the helium hold time, but 7 days was considered sufficient. A refrigerator could be easily added if a longer hold time is desired. The magnet has been ruggedly designed and can withstand 6 g's in all directions.

We have completed some preliminary designs of critical components of the circuit, including the couplers and sever. Constraints such as limited space and the need to avoid beam interception were taken into account. The input coupler converts radiation from the $TE_{1,1}$ to the $TE_{5,1}$ waveguide mode. The $TE_{1,1}$ will be transmitted to the coupler via low–loss corrugated waveguide. A schematic of the input coupler is shown in Fig. 27. It consists of a horn, a flat 'steering' mirror, a doubly curved mirror, and a helically cut quasi-optical launcher with a nonlinear downtaper to the interaction waveguide radius. The overall predicted conversion efficiency is 70%. The radiation leaving the horn is assumed to be a linearly polarized Gaussian beam. It is redirected towards the curved reflector by a flat steering mirror. The horn is assumed to have the correct E-plane and H-plane flare angles to produce the E_φ pattern shown in Fig. 28 at the doubly curved reflector. This theoretical pattern is determined using a diffraction code in the near field and it is the same pattern that would be produced by the $TE_{5,1}$ if it were launched from the quasi-optical launcher. The size of the reflector is determined by the theoretical near-field pattern and the shape of the reflector is found from geometrical optics by requiring that the rays leaving the launcher arrive at the focus of the reflector in phase. Very precise mirrors can be manufactured since the calculated shape is then placed in a format that can be understood by computer-controlled milling machines.

After leaving the doubly curved mirror, the radiation is incident on a Vlasov-type quasi-optical launcher designed for the $TE_{5,1}$ mode. The length of the straight cut of the launcher, L, is 3.447 cm and was determined by equating the energy flux through

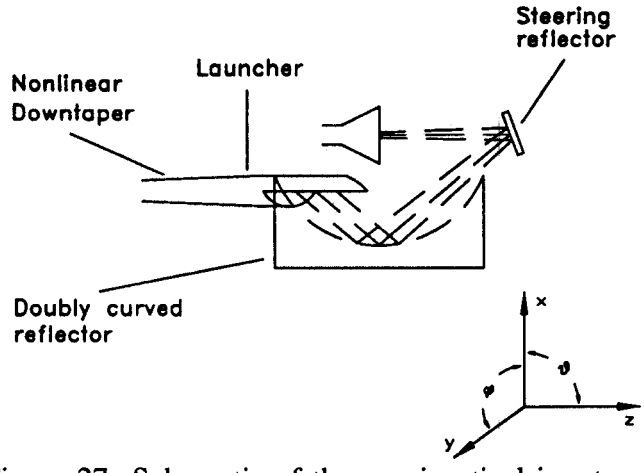

Figure 27: Schematic of the quasi-optical input coupler.

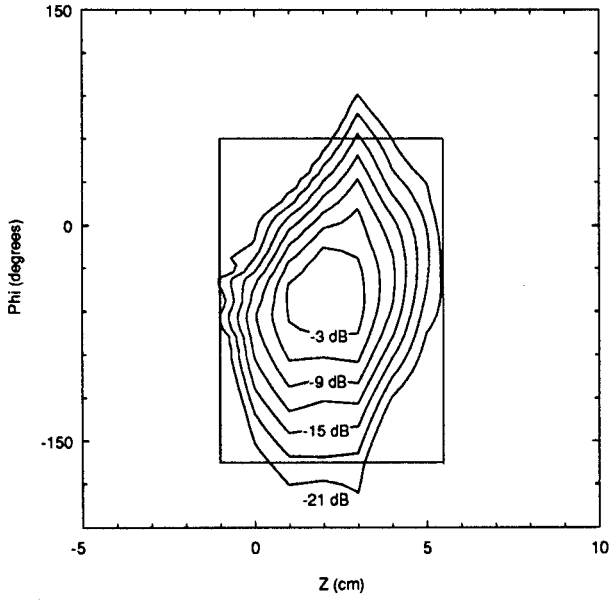

Figure 28: The E_φ near-field pattern at the curved reflector. The effective area of the mirror is outlined for reference.

Mode	Total Power (%)
$TE_{5,1}$	99.64
$TM_{5,1}$	0.33
$TM_{5,2}$	0.03

Table 7: Mode content after the nonlinear downtaper for the input coupler system.

the waveguide cross section to the energy flux through the rectangular aperture of length L and width R_w, the radius of the waveguide.

A nonlinear downtaper is used to minimize the amount of mode conversion as the waveguide radius (0.500 cm) is tapered down to the interaction waveguide radius (0.345 cm). The shape of the taper is determined from a nonlinear tapers code which also predicts the amount of expected conversion. The theoretical amount of mode conversion for this downtaper is summarized in Table 7.

The presence of competing backward wave modes will require that the circuit consist of two or three sections separated by severs. The severs must be well matched to minimize reflection, and must provide adequate isolation between the sections. After the electrons are 'bunched' by the input $TE_{5,1}$ signal in the first section, most of the rf power is allowed to escape from the guide or be absorbed in a lossy medium on the waveguide wall. If the length of the bunching region is shorter than the start-up length of the undesired modes, and if the sever is lossy enough, then a suppression of the unwanted modes is possible.

In order to investigate the effect of including a sever in the interaction region, the nonlinear code SPOT was modified to model the sever. An example of the gain history of the $TE_{5,1}$ for the tapered magnetic field case of Fig. 25 is shown in Fig. 29. Curve A shows the gain as a function of the interaction length when there is no sever present. The saturation length and power are 19.0 cm and 121.3 kW, respectively. Curves B and C show the gain when a sever is included in the model. The starting position of the sever is constrained by the starting oscillation lengths of the competing modes, and the length of the sever is determined by the ability to construct a sever with the desired loss. The sever in Fig 29 begins at z=3 cm and has a length of 2 cm.

For case B, the saturation length of the system has increased by an amount slightly larger than the sever length while the saturated power has decreased from case A. The saturated length and power for case B are 21.4 cm and 110.0 kW, respectively. The effectiveness of the modulation on the beam depends upon both the bunching of the electrons by the RF field in the first section and the inertial bunching of the electrons in the (field-free) region of the sever. Clearly, for a fixed sever length and starting position, the total bunching process in the 'system' comprised of the first section and sever section can be optimized by the amount of modulation on the beam caused in the first section by the input signal. Curve C shows the gain for an optimized input signal. The saturation length has decreased to 20.9 cm and the saturated power has increased to 119.3 kW by increasing the input power from 20 W (case B) to 33 W. This modest increase in input signal results in only a slight decrease (0.5%) in the saturated efficiency and an increase in the saturation length of 1.9 cm over the case without a sever.

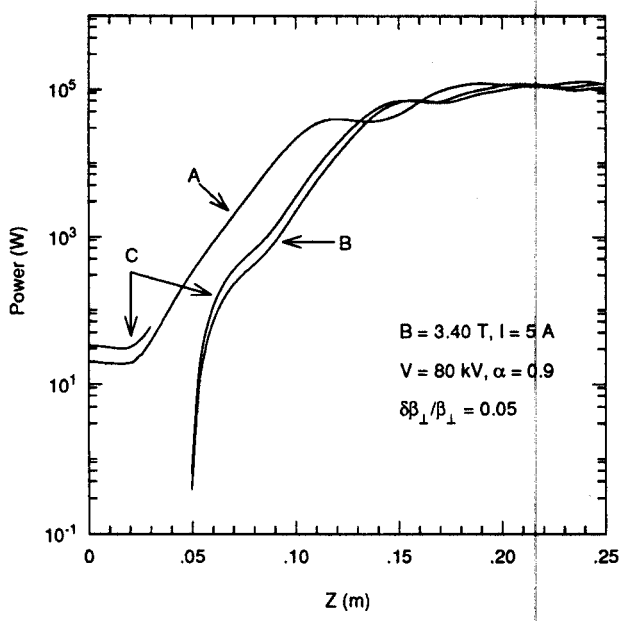

Figure 29: Gain history of the $TE_{5,1}$ in a tapered magnetic field. The gain is shown for: the case without a sever (curve A); the case with a sever 2 cm long beginning at Z=3 cm (curve B); and the case with the same sever but for optimized bunching conditions in the bunching and sever regions (curve C).

We are considering two types of severs: an open gap and resistive walls. In the

Mode	Total Power (%)
$TE_{5,1}$	97.75
$TM_{5,1}$	0.40
$TM_{5,2}$	1.85

Table 8: Mode content after the nonlinear uptaper in the open waveguide sever.

open waveguide sever the radiation is lost through a break in the waveguide. Before the waveguide sever, the radius of the interaction region is tapered up to a radius of 0.5 cm in order to reduce reflections at the abrupt discontinuity of the open ended waveguide. A nonlinear uptaper is used to minimize the mode conversion from the $TE_{5,1}$ to other radial modes. The mode mix after the uptaper is summarized in Table 8. The opening in the waveguide is 1.2 cm long and will provide over 15 dB attenuation for the $TE_{5,1}$ mode. A nonlinear downtaper is then used to decrease the waveguide radius back to 0.345 cm.

Once the $TE_{5,1}$ mode is amplified, the output coupler must convert the mode to a Gaussian beam and couple the beam out of the vacuum system. The coupler consists of a nonliner uptaper, a helically cut quasi-optical launcher, a doubly curved focusing reflector, a steering reflector, and a vacuum window. It is essentially the input coupler in reverse. The overall efficiency of conversion is $> 90\%$. A schematic of the output coupler is shown in Fig. 30.

A nonlinear uptaper is used to increase the radius of the waveguide from 0.345 cm, the radius of the interaction region, to 0.7 cm, a radius suitable for the quasi-optical launcher. The nonlinear taper was designed to produce a minimum of mode conversion from the $TE_{5,1}$ to radial modes. The mode conversion caused by the taper is summarized in Table 9.

A helically cut 'Vlasov-type' launcher is used to launch the $TE_{5,1}$ radiation at a fixed polar angle with a moderate azimuthal spread. The reflection at the launcher due to the free-space mismatch is less than 5%. The near field radiation pattern from the launcher was analyzed using a diffraction theory. The total power was found to consist of 79% E_φ, 15% E_θ and 6% E_r. The theoretical near-field E_φ pattern at the

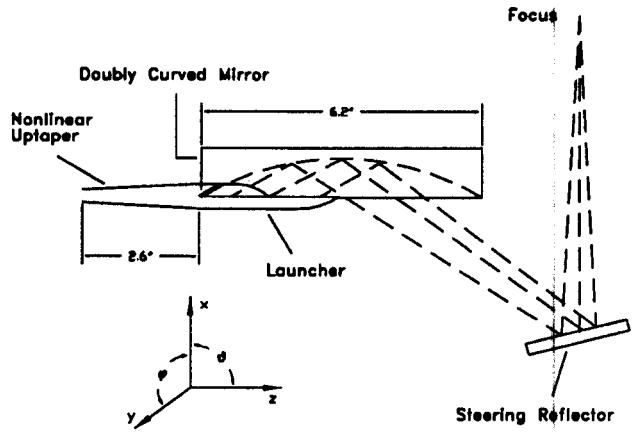

Figure 30: Schematic of the quasi-optical output coupler.

Mode	Total Power (%)
$TE_{5,1}$	97.42
$TE_{5,2}$	0.08
$TM_{5,1}$	0.82
$TM_{5,2}$	0.97
$TM_{5,3}$	0.67
$TM_{5,4}$	0.04

Table 9: Mode content after the nonlinear uptaper in the output coupler system.

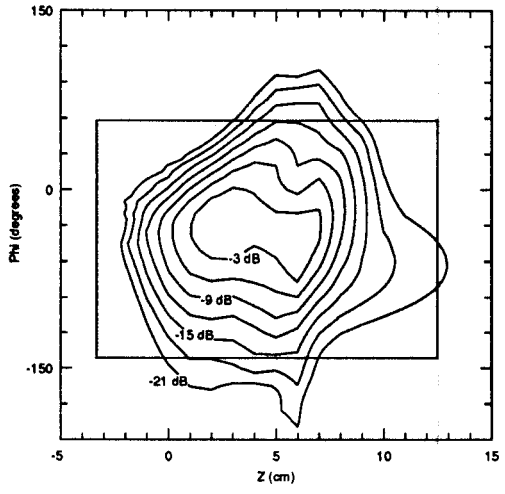

Figure 31: The E_φ near field radiation pattern for the $TE_{5,1}$ mode launcher. The point z = 0 corresponds to the z value at the center of the launcher.

approximate position of the focusing reflector is shown in Fig. 31.

The doubly curved reflector was designed to focus the radiation from the launcher into a small, Gaussian-like focus. The shape of the reflector was determined by requiring that the waves leaving the launcher have the same phase at the focus. The size of the reflector was determined by the near-field launcher pattern and is outlined for reference in Fig. 31. The reflector was designed so that the 1/e radii in the horizontal and vertical planes of the focusing beam are equal to ensure a high quality Gaussian beam with no astigmatism. The radiation leaves the curved reflector and is redirected by the the flat steering mirror towards the output window. The output window is tilted at the Brewster angle to allow the focused radiation to leave the vacuum system with minimal reflection.

5 Summary

A detailed design study of a 95 GHz gyrotron amplifier has been completed. The most promising design is based on fundamental ($\omega \approx \omega_c$) operation in the $TE_{5,1}$ whispering gallery mode using a magnetron injection electron gun (MIG). Operating parameters can be found in Table 5 of this report. This design is particularly attractive because it can produce much higher powers (125 kW) than presently available sources, such as the coupled cavity TWT, while maintaining low ohmic losses in the interaction circuit. Other advantages include a relatively low operating voltage (80 kV), adequate beam clearance, and a simple and robust microwave structure for increased reliability. Efficiencies up to 31% are possible with a tapered magnetic field, and could be further increased with a depressed collector. This device is capable of the high average powers, high gain (38 dB), and large bandwidth (> 5 GHz) required for high resolution radar systems.

The $TE_{5,1}$ mode was selected after completion of a parametric study and computer simulations of potential electron guns. Required specifications, in addition to high power and efficiency, included a 5 GHz bandwidth, a saturated gain of 30 dB, and constraints on the weight, size, and input power. Our emphasis was on fundamental operation with waveguide circuits based on electron guns presently available at MIT. Such circuits have been successfully used to produce efficient, high power oscillators at high frequency. Calculations were made of the circuit dimensions, beam coupling to the rf field, current density and space charge forces, and wall clearance. Beam stability was evaluated by determining the upper limits on $\alpha = v_\perp / v_{||}$ based on absolute instabilities, and by calculating the starting conditions of potential competing backward wave (BW) modes.

We completed detailed simulations of two types of electron guns: a Pierce gun with a magnetic wiggler that produces an on-axis beam, and a magnetron injection gun (MIG). These models included the effects of self- fields and space charge on the beam quality. The Pierce gun can couple to low order $TE_{1,p}$ modes, resulting in reduced competition. However, the small beam radius needed to achieve good rf coupling results in a high current density (>1000 A/cm^2), which leads to excessive velocity spreads in the beam compression region prior to the circuit. The observation of large velocity spreads in Pierce-wiggler guns induced by internal space charge forces is a new result not seen in previous simulations. Although techniques may exist to avoid this problem, a major study of the wiggler design would be required. The MIG is more compact and lighter than the Pierce gun, and allows independent control of the cathode voltage and current. The gun we studied has been used at MIT to generate

up to 150 kW of rf power at 140 GHz with an efficiency of 37%. The MIG produces an annular beam with a low current density and avoids the space charge problems of the Pierce gun. Simulations from the cathode to the circuit based on the American Magnetics, Inc.(AMI) magnet design indicate perpendicular spreads below 5% are possible at 95 GHz. Based on these factors, we selected the MIG for the final design.

Our parametric study indicated that the MIG can be used at 95 GHz with a variety of modes. The most promising were whispering gallery modes such as the $TE_{5,1}$. These provided the strongest coupling to the beam and had fewer competing modes. They have been successfully used in high frequency, megawatt oscillators. These modes can also be used with Vlasov launchers for input and output coupling. Experiments have demonstrated that such launchers can have efficiencies in excess of 95%. A nonlinear, self-consistent code was used to calculate the operating parameters of the $TE_{5,1}$ mode at saturation. A finite beam thickness and a perpendicular velocity spread of 5% were assumed. The need to avoid absolute instabilites in the circuit necessitated a low velocity ratio ($\alpha < 1$). In spite of this limitation, powers up to 86 kW are predicted for a uniform magnetic field. The high linear gain (5.0 dB/cm) leads to a short circuit length which is less susceptible to degradation due to velocity spread. A substantial improvement in performance is possible by using a modest linear downtaper of the magnetic field (from 3.4 T to 3.2 T) over the latter half of the circuit. This leads to output powers of 125 kW and efficiencies of 31% without a loss of bandwidth.

Although operation in whispering gallery modes does reduce the number of competing modes and improve the stability of the amplifier, some competition from BW modes is anticipated. The use of severs, either resistive or quasi-optical, will be required to suppress these oscillations. Severs have been successfully used in both conventional and fast wave devices and should only cause a modest reduction in the performance of our design. It may also be possible to perturb the competing modes so they are less resonant with the beam. A coaxial insert could be used to damp volume modes while leaving the desired mode unaffected. The other area of concern is oscillations due to feedback and reflections. The use of quasi-optical couplers in the $TE_{5,1}$ design should minimize this problem by isolating the sources of such reflections, such as the window, from the circuit. Nonlinear tapers have been used in the circuit to reduce further reflections.

Harmonic operation was also considered as a design option. The main motivation was to reduce the cavity magnetic field and shielding requirements. Operation at second or third harmonic would still require a superconducting (SC) magnet. The magnet size, which is predominantly determined by the helium reservoir, would be

reduced only slightly. To use permanent magnets would require fourth harmonic operation. The risk for such a design would be high. Predicted efficiencies are low, and competition from modes at other harmonics would be severe. A higher field gradient at the beam would be needed to increase the efficiency. This would require placing the circuit near the beam, which would lead to unacceptable beam interception. Although SC magnet technology has its uncertainties, the AMI design shows that a compact, light, and robust magnet is possible. Therefore, we believe a fundamental design with sufficient shielding is the optimum approach.

A final mechanical design based on fundamental $TE_{5,1}$ operation and using the AMI magnet was completed. A schematic of the design can be found in Fig. 8. The overall system is under four feet in height and meets the weight specifications. The four inch warm bore provides sufficient room for the circuit and input coupler. The input coupler consists of an inverse Vlasov launcher and mirror illuminated by a horn propagating the $TE_{1,1}$ mode. The coupler is compact and easily fits between the gun and circuit. The ouput coupler is based on the same approach, but must be somewhat larger to accomodate the high output powers and provide clearance for the beam. The collector is a separate component, and could be depressed to increase the efficiency.

References

[1] K.E. Kreischer, T.L. Grimm, W.C. Guss, R.J. Temkin, and K.Y Xu. High frequency gyrotrons for ECRH: progress at MIT. In , page , 1990.

[2] V.L. Granatstein and P. Sprangle and M. Herndon and R.K. Parker and S.P. Schlesinger. *J. Appl. Phys.*, 46:3800–05, 1975.

[3] L.R. Barnett and K.R. Chu and J.M. Baird and V.L. Granatstein and A.T. Drobot. *IEEE IEDM Digest*, 164–67, 1979.

[4] L.R. Barnett, Y.Y. Lau, K.R. Chu, and V.L. Granatstein. An experimental wide-band gyrotron traveling-wave amplifier. *IEEE Trans. on Electron Devices*, 28:872–75, 1981.

[5] G.S. Park, V.L. Granatstein, P.E. Latham, C.M. Armstrong, A.K. Ganguly, and S.Y. Park. Phase stability of gyroklystron amplifier. *IEEE Trans. Plasma Science*, 19:632–40, 1991.

[6] W.M. Bollen, A.H. McCurdy, B. Arfin, R.K. Parkter, and A.K. Ganguly. *IEEE Trans. Plasma Science*, 13:417–23, 1985.

[7] L.R. Barnett, L.H. Chang, H.Y. Chen, K.R. Chu, W.K. Lau, and C.C. Tu. Absolute instability competition and suppression in a millimeter-wave gyrotron traveling-wave tube. *Phys. Rev. Lett.*, 63:1062–65, 1989.

[8] P. Ferguson and R. Symon. *IEEE IEDM Digest*, 310–13, 1980.

[9] K.R. Chu and A.T. Lin. Gain and bandwidth of the gyro-TWT and CARM amplifiers. *IEEE Trans. Plasma Science*, 16:90–104, 1988.

[10] Y.Y. Lau, K.R. Chu, L.R. Barnett, and V.L. Granatstein. *Int. J. Infrared and Millimeter Waves*, 2:373–93, 1989.

[11] J.A. Davies. Conditions for absolute instability in the cyclotron resonance maser. *Phys. Fluids*, B1:663–69, 1989.

[12] R.J Briggs. Electron stream interactions with plasmas. In , chapter , page , 1964.

[13] S.Y. Park, V.L. Granatstein, and R.K Parker. A linear theory and design study for a gyrotron backward–wave oscillator. *Int. J. Electronics*, 57(6):1109–1123, 1984.

[14] V.L. Bratman and M.A. Moiseev. Conditions for self-excitation of a cyclotron resonance maser with a nonresonant electrodynamic system. *Radiophys. Quantum Elect.*, 18:772–79, 1975.

[15] A.W. Fliflet. Linear and non-linear theory of the doppler-shifted cyclotron resonance maser based on TE and TM waveguide modes. *Int. J. Electronics*, 61:1049–80, 1986.

[16] G.S. Nusinovich and H. Li. Theory of gyro-traveling waves tubes at cyclotron harmonics. *Submitted to Int. J. Electronics*, 1991.

[17] R.J. Temkin, K.E. Kreischer, W.J. Mulligan, S. MacCabe, and H.R. Fetterman. A 100 kW, 140 GHz pulsed gyrotron. *Int. J. Infrared and Millimeter Waves*, 3:427–37, 1982.

[18] K.R. Chu, L.R. Barnett, W.K. Lau, and L.H. Chang. Recent developments in millimeter wave gyro–TWT research at NTHU. *IEDM Technical Digest*, 699–702, 1990.

[19] N.S. Ginzburg, N.Yu. Peskov, and M.D. Tokman. Formation of a helical relativistic electron beam in a system with a periodic undulator and a weakly nonuniform longitudinal magnetic field. *Soviet Tech. Phys. Lett.*, 36:75–79, 1991.

[20] B.G. Danly, K.D. Pendergast, and R.J. Temkin. Theory and design of a high-power, 140 GHz CARM amplifier. *SPIE*, 873:143–47, 1988.

[21] A.K. Ganguly and K.R. Chu. Limiting current in gyrotrons. *Int. J. Infrared and Millimeter Waves*, 5:103–122, 1984.